

A Comprehensive Study of Czernik 41 and NGC 1342 Using CCD UBV and Gaia DR3 Data

BURÇIN TANIK ÖZTÜRK,¹ SELÇUK BILIR,² TALAR YONTAN,² OLCAY PLEVNE,² TANSEL AK,^{2,3} SERAP AK,²
REMZIYE CANBAY,¹ AND TIMOTHY BANKS^{4,5}

¹*Istanbul University, Institute of Graduate Studies in Science, Programme of Astronomy and Space Sciences, 34116, Istanbul, Turkey*

²*Istanbul University, Faculty of Science, Department of Astronomy and Space Sciences, 34119, Beyazıt, Istanbul, Turkey*

³*Istanbul University, Observatory Research and Application Center, Istanbul University, 34119, Istanbul, Turkey*

⁴*Nielsen, 675 6th Ave, New York, NY 10011, USA*

⁵*Departments of Physical Science and Engineering, Harper College, 1200 W Algonquin Rd, IL 60067, USA*

ABSTRACT

In this study, the structural, astrophysical, kinematic, and Galactic orbital parameters of the open clusters Czernik 41 and NGC 1342, as well as their dynamical evolution, are investigated using CCD UBV photometry and *Gaia* data. By applying the UPMASK algorithm to *Gaia* astrometric data for the estimation of cluster membership probabilities, we have determined that 382 stars in Czernik 41 and 111 stars in NGC 1342 exhibit the highest statistical likelihood of being cluster members. Fundamental parameters (including reddening, metallicity, distance, and age) were derived using both classical methods, where parameters are determined separately, and Markov Chain Monte Carlo (MCMC) methods, where parameters are estimated simultaneously. The results obtained from both approaches are in agreement, confirming the reliability of the derived parameters and demonstrating their robustness against potential degeneracies. The distances to Czernik 41 and NGC 1342 were determined as 2485 ± 151 pc and 645 ± 42 pc, respectively, while their ages were estimated to be 69 ± 10 Myr and 1000 ± 50 Myr. The metallicity values ($[Fe/H]$) were found to be 0.07 ± 0.09 dex for Czernik 41 and -0.14 ± 0.07 dex for NGC 1342. The stellar mass functions for both clusters were derived, yielding slopes of $\Gamma = 1.67 \pm 0.23$ for Czernik 41 and $\Gamma = 1.56 \pm 0.41$ for NGC 1342. Kinematic orbit analysis indicates that Czernik 41 originated within the Solar circle, whereas NGC 1342 formed outside it.

Keywords: Galaxy: open cluster and associations: individual: Czernik 41 and NGC 1342 (1160), stars: Hertzsprung-Russell (HR) diagram (725), Galaxy: Stellar kinematics (1608)

1. INTRODUCTION

Open clusters (OCs) are essential stellar systems for exploring the processes of star formation, stellar evolution, and the structural dynamics of the Galactic disc. These relatively young and metal-rich systems are typically located near the Galactic plane and consist of stars that share similar physical properties, such as age and chemical composition, despite significant differences in mass (Lada & Lada 2003; Maurya & Joshi 2020). Formed through the collapse of molecular clouds, the stars within OCs initially remain gravitationally bound, exhibiting coherent positional and kinematic traits (McKee & Ostriker 2007). These unique characteristics make OCs indispensable for understanding the broader

mechanisms of stellar evolution and dynamics in the Milky Way.

Photometric and astrometric studies have been proven crucial for determining fundamental properties of OCs, including age, distance, and metallicity. Such parameters, often inaccessible for single stars, are derived through the collective analysis of cluster members (Dias et al. 2021). Recent advancements in astrometric precision, particularly through the *Gaia* mission (Gaia Collaboration et al. 2016) data releases, have enhanced our ability to trace the motions of OC members, enabling detailed reconstruction of their orbits and Galactic dynamics (Tarricq et al. 2021; Rangwal et al. 2024; Çınar et al. 2024; Çakmak et al. 2024; Taşdemir et al. 2025). These datasets have revealed systematic variations in the properties of OCs by location, providing clearer pictures of star formation and the chemical evolution of the

Galactic disc (Sestito et al. 2008; Frinchaboy et al. 2013; Reddy et al. 2020).

The dynamic evolution of OCs is another key area of research, with studies indicating that most clusters dissolve within a few hundred million years due to tidal interactions, stellar feedback, and encounters with giant molecular clouds (Portegies Zwart et al. 2010). Despite their ephemeral nature, the kinematic imprints of dissolved clusters contribute significantly to the stellar population of the Galactic disk. Investigating these dynamics offers insights into the processes governing stellar migration and the distribution of stellar populations across the Milky Way (Piskunov et al. 2006; Bastian & Lardo 2018). Furthermore, the internal dynamics of OCs or globular clusters, such as mass segregation and binary star interactions, play critical roles in determining their evolutionary trajectories (cf. Spitzer 1987). The role of OCs in tracing the Galactic structure is increasingly being recognized. By combining their astrophysical properties with their kinematic data, researchers have successfully mapped the spiral arms (Castro-Ginard et al. 2021; Hao et al. 2021), warp (Vázquez et al. 2010; Hidayat et al. 2019), and radial metallicity gradients of the Milky Way (Netopil et al. 2022; Spina et al. 2022; Joshi et al. 2024). Such studies provide valuable constraints on the formation and evolution of the Galactic disk, revealing the interplay between star formation, chemical enrichment, and dynamical processes.

Within the scope of the systematic OC surveys that we initiated approximately 15 years ago (c.f. Bilir et al. 2010; Yontan et al. 2015; Bostancı et al. 2015; Ak et al. 2016), we combine *UBV* photometric data with the high-precision astrometric and radial velocity measurements provided by the *Gaia* satellite. This approach enables us to analyze the structural, astrophysical, kinematical, and dynamical orbital properties of OCs, thereby allowing us to investigate their birthplaces. In this study, we focus on Czernik 41 and NGC 1342 to expand our understanding of relatively unexamined OCs in the Galaxy. Due to their proximity to the Galactic plane, these OCs are significantly influenced by the presence of field stars, necessitating the application of statistical methods to mitigate field contamination. This investigation represents a continuation of a systematic research initiative on under-explored OCs, contributing to a broader understanding of Galactic structure and evolution (Yontan et al. 2019, 2021, 2022; Yontan 2023a; Banks et al. 2020; Akbulut et al. 2021; Koç et al. 2022; Gokmen et al. 2023). By employing CCD *UBV* photometric data in conjunction with the most up-to-date datasets provided by the *Gaia* mission, we aim to derive the fundamental

parameters of Czernik 41 and NGC 1342 with improved precision.

Czernik 41 ($\alpha = 19^{\text{h}}51^{\text{m}}01^{\text{s}}.0$, $\delta = +25^{\circ}17'24.0''$, $l = 62^{\circ}0238$, $b = -00^{\circ}6899$) was identified by Czernik (1966) following examination of the Palomar Sky Atlas. It was classified by Ruprecht (1966) as Trumpler type IV3m, denoting a very loose, low-density cluster of a wide range in stellar brightness and having a moderate number of member stars, although with the additional comment of ‘doubtful’. Maciejewski & Niedzielski (2007) included it in their *BV* CCD survey of 42 clusters, which derived estimates for the limiting and core radii through King (1962) radial density profile fits as well as extinction, ages, and distances via isochrone fitting. Values for the parameter estimates relevant to the current study are given in Table 1, which also contains key estimates from later papers discussed in this paragraph. Kharchenko et al. (2012) and Kharchenko et al. (2013) analyzed 2MASS infrared photometry (Skrutskie et al. 2006), combined with PPMXL (Roeser et al. 2010) positions and proper motions, of 642 OCs in the second Galactic quadrant. They derived estimates for spatial parameters (such as cluster radii), distances, ages, and reddening through profile and isochrone fitting. Dias et al. (2014) presented a catalog of 724 clusters, providing the mean proper motions and membership probabilities of stars located in the direction of the clusters based on the second U.S. Naval Observatory CCD Astrometry Catalog (UCAC2, Zacharias et al. 2004). Loktin & Popova (2017) included the ages, distances, and color excesses of 496 OCs in their catalog, which was based on their redeterminations from published photometry (including 2MASS). Cantat-Gaudin et al. (2018) compiled a catalog of 1,229 open clusters, including Czernik 41, deriving fundamental parameters based on *Gaia* DR2 (Gaia Collaboration et al. 2018) data combined with an application of the UPMASK (Krone-Martins & Moitinho 2014) technique to assign membership probabilities for stars in the sight lines of the clusters (identified from a literature review). Subsequent studies (Liu & Pang 2019; Cantat-Gaudin et al. 2020; Cantat-Gaudin & Anders 2020; Tarricq et al. 2021) made use of the proper motions and supplemented them with new estimates of the cluster age, metallicity, distance, and radial velocity. For example, Dias et al. (2021) presented an analysis of the *Gaia* DR2 data for 1,743 OCs (again deriving distance, age, and extinction), while Tarricq et al. (2021) presented weighted mean velocities and galactic orbital parameters for 1,382 OCs based on *Gaia* DR2 radial velocities and literature data. Other studies, such as Medina et al. (2021); Zhou & Chen (2021); Hao et al. (2022) were interested in a cepheid belonging to Czernik 41.

NGC 1342 ($\alpha = 03^{\text{h}}31^{\text{m}}34^{\text{s}}.6$, $\delta = +37^{\circ}22'48''$, $l = 154^{\circ}9402$, $b = -15^{\circ}3463$) was discovered by William Herschel on 28 December 1799 (Herschel 1802), including it into his sixth list of objects (“coarsely scattered clusters of stars”), noting an about 15 arcminute diameter. The cluster is included in the “Herschel 400” list popular with amateur astronomers. Given the size of the cluster and its early discovery, it has been included in many studies and catalogs (although there are only a handful of comprehensive studies of the cluster). Table 1 lists parameter estimates, relevant to the current paper, from the literature. A few key studies are described further in this paragraph. The cluster was classified by Ruprecht (1966) as a Trumpler type III3p, which indicates a loosely structured, low-density cluster with a wide range of stellar brightness and a relatively small number of member stars. Peña et al. (1994) estimated the age (4×10^8 yr), distance (530 ± 118 pc), and reddening ($E(b - y) = 0.297 \pm 0.112$) of the cluster based on their *uvby- β* photometry, noting ‘patchy’ extinction across NGC 1342. Reddy et al. (2015) collected high-dispersion echelle spectra of three red giant members of NGC 1342, estimating their radial velocities and composition, along with age (of 0.5 Gyr) via isochrone fits using photometry from Hoag et al. (1961). Sarajedini et al. (1995) mentions in a BAAS summary their *BVI* observations and subsequent color-magnitude diagrams of the cluster, but, unfortunately, do not appear to have further published their results. Cantat-Gaudin et al. (2018) applied the data and methodology described above for Czernik 41 to NGC 1342, leading to estimates used in many later catalogs. Similarly, Dias et al. (2021) included the cluster in their study.

In this study, we analyzed the OCs Czernik 41 and NGC 1342 by determining the membership probabilities of their stars, mean proper motions, and distances. Our analysis combines ground-based *UBV* photometric observations with high-precision astrometry and photometry data from the *Gaia* third data release (*Gaia* DR3) (Gaia Collaboration et al. 2023). We report the fundamental parameters, luminosity and mass functions, the dynamical properties of mass segregation, and the kinematic and Galactic orbital properties of both OCs.

2. OBSERVATIONS

The CCD *UBV* photometric observations for the OCs Czernik 41 and NGC 1342 were conducted on 2020 July 21 and 2019 September 29, respectively. These observations utilized the 100-cm *f*/10 Ritchey-Chrétien telescope (T100) at the TÜBİTAK National Observa-

tory (TUG)¹ in Turkey. Imaging was performed with a back-illuminated 4k×4k pixel CCD, providing an image scale of 0''31 pixel⁻¹ and a total field of view of 21'5 × 21'5. The CCD specifications included a gain of 0.55 e⁻ ADU⁻¹ and a readout noise of 4.19 e⁻. Identification charts for the OCs are shown in Figure 1, and a detailed observation log is provided in Table 2. Shorter exposure times were used to obtain unsaturated images of brighter stars, while longer exposures facilitated accurate photometry for fainter stars. For photometric calibration, standard stars from Landolt (2009) were observed on the same nights as the clusters. A total of 14 Landolt fields were observed across an airmass range of 1.233 to 2.061, comprising 97 standard stars (Table 3). Technical information on the observing conditions of the TUG site can be found in Ak et al. (2024). The raw science images underwent standard bias subtraction and flat fielding using IRAF². The instrumental magnitudes of the Landolt (2009) standard stars were derived using IRAF’s aperture photometry tools. Multiple linear regression analysis of these magnitudes yielded photometric extinction and transformation coefficients for the two observing nights, which are presented in Table 4. For cluster images, astrometric corrections were performed using PyRAF³ and astrometry.net⁴. Instrumental magnitudes of objects within the cluster regions were measured using Source Extractor and PSF Extractor routines (Bertin & Arnouts 1996), with aperture corrections subsequently applied. Finally, instrumental magnitudes were transformed to standard *UBV* magnitudes based on the transformation equations provided by Janes et al. (2013)

$$\begin{aligned} v &= V + \alpha_{bv}(B - V) + k_v X + C_{bv}, \\ b &= V + \alpha_b(B - V) + k_b X + k'_b X(B - V) + C_b, \\ u &= V + (B - V) + \alpha_{ub}(U - B) + k_u X + k'_u X(U - B) \\ &\quad + C_{ub} \end{aligned} \tag{1}$$

In the above equations, U , B , and V are the magnitudes in the standard photometric system. u , b , and v indicate the instrumental magnitudes. X is the airmass. k and k' represent primary and secondary extinction coefficients. α and C are the transformation coefficients to the standard system and zero points, respectively.

¹ www.tug.tubitak.gov.tr

² IRAF was distributed by the National Optical Astronomy Observatories

³ PyRAF is a product of the Space Telescope Science Institute, operated by AURA for NASA

⁴ http://astrometry.net

Table 1. Fundamental parameters for Czernik 41 and NGC 1342 obtained in this study and compiled from the literature: Color excess ($E(B - V)$), distance (d), iron abundance ($[\text{Fe}/\text{H}]$), age (t), proper-motion components ($\langle \mu_\alpha \cos \delta \rangle$, $\langle \mu_\delta \rangle$), radial velocity (V_R), and reference (Ref).

Czernik 41							
$E(B - V)$ (mag)	d (pc)	$[\text{Fe}/\text{H}]$ (dex)	t (Myr)	$\langle \mu_\alpha \cos \delta \rangle$ (mas yr ⁻¹)	$\langle \mu_\delta \rangle$ (mas yr ⁻¹)	V_R (km s ⁻¹)	Ref
$1.28^{+0.14}_{-0.17}$	1360^{+400}_{-650}	—	500	—	—	—	(1)
1.280	1540	—	300	-1.34	-3.30	—	(2)
—	—	—	—	-2.49 ± 5.08	-2.60 ± 1.22	—	(3)
1.336	3032	—	30	-1.250 ± 0.659	-2.863 ± 0.676	—	(4)
—	2511^{+16}_{-17}	—	—	-2.932 ± 0.138	-6.164 ± 0.128	—	(5)
—	786 ± 450	—	100	-2.900 ± 0.230	-6.072 ± 0.297	—	(6)
1.326	2543	—	13	-2.932 ± 0.138	-6.164 ± 0.128	—	(7)
—	2511^{+16}_{-17}	—	—	-2.932 ± 0.138	-6.164 ± 0.128	—	(8)
1.237 ± 0.008	2620 ± 212	0.002 ± 0.108	6 ± 1	-2.937 ± 0.137	-6.153 ± 0.128	-13.40 ± 0.53	(9)
—	2451	—	14	-2.932 ± 0.138	-6.164 ± 0.128	-2.41 ± 11.67	(10)
1.500 ± 0.035	2485 ± 151	0.07 ± 0.09	69 ± 10	-2.963 ± 0.068	-6.163 ± 0.101	2.41 ± 1.92	(11)
NGC 1342							
$E(B - V)$ (mag)	d (pc)	$[\text{Fe}/\text{H}]$ (dex)	t (Myr)	$\langle \mu_\alpha \cos \delta \rangle$ (mas yr ⁻¹)	$\langle \mu_\delta \rangle$ (mas yr ⁻¹)	V_R (km s ⁻¹)	Ref
0.42	610	-0.163	—	—	—	—	(12)
—	550	-0.44	—	—	—	—	(13)
—	550	-0.38	300	—	—	—	(14)
0.401 ± 0.151	530 ± 118	—	400	—	—	—	(15)
—	665	—	—	-0.12 ± 0.27	-3.10 ± 0.37	—	(16)
0.32	665	—	160	0.13 ± 0.80	2.72 ± 0.77	-10.90 ± 0.30	(17)
—	—	—	—	—	—	-10.67 ± 0.11	(18)
0.331	665	-0.160	400	-3.12	-5.50	-11.50 ± 0.40	(02)
—	—	—	—	-2.99 ± 2.45	-1.82 ± 1.76	—	(03)
—	665 ± 133	-0.14 ± 0.05	452	-1.15 ± 0.087	-2.80 ± 0.87	-10.67 ± 0.11	(19)
0.345	667	—	452	-2.704 ± 0.413	-8.046 ± 0.386	-11.50 ± 0.40	(04)
—	665	-0.160	160	0.13 ± 0.80	-2.72 ± 0.077	-10.90 ± 0.10	(20)
—	$653^{+1.0}_{-0.7}$	—	—	0.520 ± 0.233	-1.604 ± 0.195	—	(05)
9.95	$653^{+1.0}_{-0.7}$	—	—	0.520 ± 0.273	-1.595 ± 0.254	—	(21)
—	668 ± 25	—	871	0.516 ± 0.004	-1.172 ± 0.004	—	(06)
0.331	665	-0.205	400	0.520 ± 0.233	-1.604 ± 0.195	-18.85	(22)
0.229	686	—	813	0.520 ± 0.233	-1.604 ± 0.195	—	(07)
—	653^{+46}_{-40}	—	—	0.520 ± 0.233	-1.604 ± 0.195	—	(08)
0.396 ± 0.053	626 ± 19	-0.115 ± 0.030	580 ± 190	0.523 ± 0.264	-1.598 ± 0.242	-9.41 ± 1.06	(09)
—	675	—	850	0.520 ± 0.233	-1.604 ± 0.195	-10.35 ± 0.19	(10)
0.270 ± 0.043	645 ± 42	-0.14 ± 0.07	1000 ± 50	0.419 ± 0.041	-1.662 ± 0.031	-10.48 ± 0.20	(11)

(1) Maciejewski & Niedzielski (2007), (2) Kharchenko et al. (2013), (3) Dias et al. (2014), (4) Loktin & Popova (2017), (5) Cantat-Gaudin et al. (2018), (6) Liu & Pang (2019), (7) Cantat-Gaudin et al. (2020), (8) Cantat-Gaudin & Anders (2020), (9) Dias et al. (2021), (10) Tarricq et al. (2021), (11) This study, (12) Cameron (1985), (13) Strobel (1991a), (14) Strobel (1991b), (15) Peña et al. (1994), (16) Loktin & Beshenov (2003), (17) Kharchenko et al. (2005), (18) Mermilliod et al. (2008), (19) Reddy et al. (2015), (20) Conrad et al. (2017), (21) Soubiran et al. (2018), (22) Zhong et al. (2020)

3. DATA ANALYSIS

3.1. Photometric Data

Photometric catalogs were constructed for stars in the directions of Czernik 41 and NGC 1342. These include the stars' equatorial coordinates (α, δ), V magnitudes, and $U - B$ and $B - V$ color indices, along with associated uncertainties. The relevant catalog for Czernik 41 contains data for 2,527 stars with apparent magnitudes in the range $9 < V$ (mag) < 22.5 , while the catalog

for NGC 1342 includes 906 stars with magnitudes spanning $8 < V$ (mag) < 22.5 . To further characterize these clusters, catalogs based on *Gaia* DR3 data (Gaia Collaboration et al. 2023) were compiled to investigate the clusters' positions in the *Gaia* photometric color spaces, compute membership probabilities, and compare cluster distances derived from photometric and trigonometric parallaxes. The *Gaia* catalogs include stars within a $40' \times 40'$ radius of the clusters' central coordinates, as adopted from Cantat-Gaudin et al. (2020). These cata-

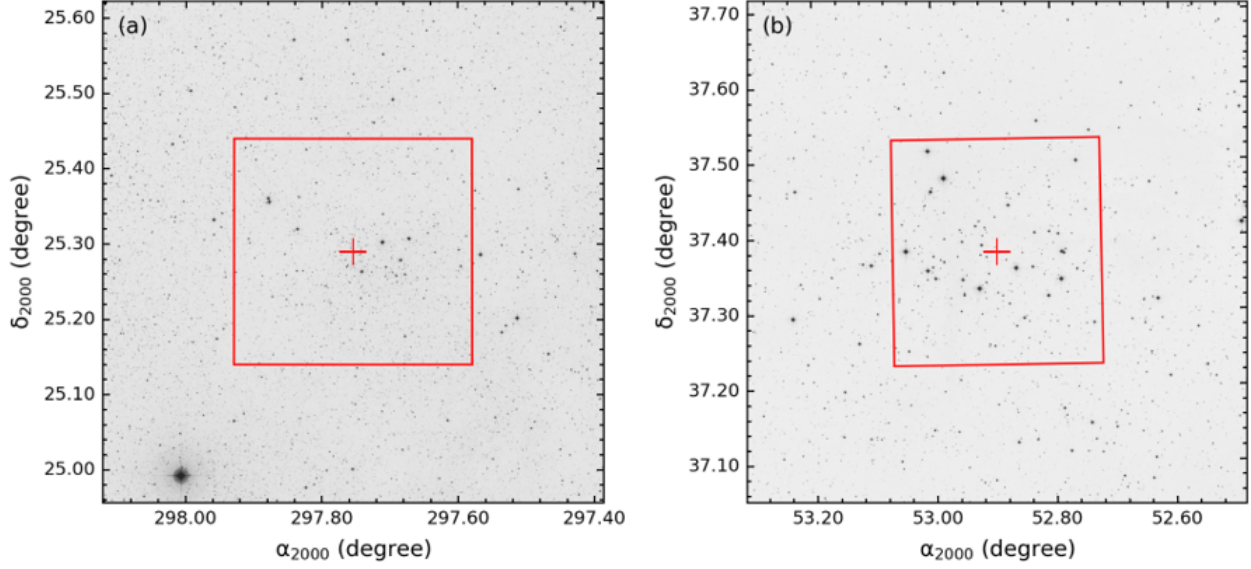


Figure 1. Star fields for Czernik 41 (a) and NGC 1342 (b) in the equatorial coordinate system. The red boundaries indicate the fields observed with the T100 telescope. North and east correspond to the up and left directions, respectively.

Table 2. Observational data for both OCs. The table includes the cluster names, observation dates (day-month-year), and the filters of the photometric *UBV* system used. For each filter, the rows specify the exposure times (in seconds) along with the corresponding number of exposures (N).

Filter/Exp, Time (s) $\times N$		
<i>U</i>	<i>B</i>	<i>V</i>
Czernik 41		
Observation Date: 21-07-2020		
80 \times 4	8 \times 6	2 \times 10
1800 \times 2	100 \times 5	20 \times 5
1500 \times 3	600 \times 3	300 \times 4
NGC 1342		
Observation Date: 29-09-2019		
60 \times 3	6 \times 5	4 \times 5
600 \times 3	60 \times 5	40 \times 5
1800 \times 3	600 \times 3	400 \times 3

logs provide photometric data (G , G_{BP} , G_{RP}), proper-motion (PM) components ($\mu_{\alpha} \cos \delta$, μ_{δ}), trigonometric parallaxes (ϖ), radial velocities (V_R), and their corresponding uncertainties, which are listed in Table 5. The *Gaia* DR3 catalog for Czernik 41 includes 217,879 stars within the magnitude range $5 < G$ (mag) < 22.5 , while the catalog for NGC 1342 contains 20,820 stars with magnitudes between $7 < G$ (mag) < 22 . Figure 1 (on page 5) displays the $40' \times 40'$ cluster fields in the *Gaia*

Table 3. Selected Landolt (2009) standard star fields. The columns denote the observation date (day-month-year), star field name from Landolt, the number of standard stars (N_{st}) observed in a given field, the number of observations for each field (N_{obs}), and the airmass range the fields were observed over.

Observation Date: 29.09.2019		
Air Mass: 1.244–1.864		
Star Field	N_{st}	N_{obs}
SA93	4	1
SA106	2	1
SA107	7	1
SA108	2	2
SA110SF2	10	1
SA111	5	1
SA112	6	1
SA113	15	1
SA114	5	1
Observation Date: 21.07.2020		
Air Mass: 1.233–2.061		
SA92SF2	15	1
SA93	4	1
SA96	2	1
SA98	19	1
SA108	2	1
SA109	2	1
SA109SF2	3	1
SA110SF2	10	1
SA111	5	1
SA112	6	1
SA113	15	1
SA114	5	1

system, with the coverage of the *UBV* data highlighted

Table 4. Transformation and extinction coefficients obtained for the two observation nights: k and k' are the primary and secondary extinction coefficients, while α and C are the transformation coefficients and zero points, respectively. Dates are day-month-year.

Observation Date: 21.07.2020				
Filter/color	k	k'	α	C
U	0.533 ± 0.124	-0.322 ± 0.098	—	—
B	0.307 ± 0.052	-0.106 ± 0.040	1.057 ± 0.064	2.089 ± 0.079
V	0.119 ± 0.018	—	—	—
$U - B$	—	—	1.304 ± 0.157	4.421 ± 0.182
$B - V$	—	—	0.071 ± 0.009	2.202 ± 0.025
Observation Date: 29.09.2019				
U	0.471 ± 0.074	0.101 ± 0.114	—	—
B	0.298 ± 0.061	-0.004 ± 0.072	0.900 ± 0.107	1.783 ± 0.091
V	0.175 ± 0.020	—	—	—
$U - B$	—	—	0.684 ± 0.166	4.176 ± 0.110
$B - V$	—	—	0.062 ± 0.008	1.834 ± 0.032

by red boundaries. Membership probabilities (P) for the cluster stars were derived from the astrometric data in the *Gaia* DR3 catalogs and incorporated into the final *Gaia* cluster catalogs. To ensure consistent analysis, stars in the *Gaia* catalogs were cross-matched with those in the *UBV* catalogs using a maximum separation limit of $8''$. This allowed the determination of membership probabilities for the stars to be included in the cluster analysis based on the *UBV* system.

To determine the precise fundamental parameters of the clusters, the photometric measurements were examined prior to the analysis to establish the faint magnitude limits for the stars in the cluster regions. These limits, known as photometric completeness limits, indicate the sensitivity of photometric measurements based on the exposure times used in the observations. The same method was applied to define the photometric completeness limits in both the *UBV* and *Gaia* systems. Histograms of the star count as a function of apparent magnitudes (V and G) were created for the stars present in the two catalogs. The magnitude at which the number of stars reaches its maximum in these distributions was adopted as the completeness limit for V and G magnitudes. The histograms for the V and G apparent magnitudes of stars in the cluster fields are presented in Figure 2. Panels (a) and (c) show the distributions of star counts as a function of V magnitudes for Czernik 41 and NGC 1342, respectively. In the case of Czernik 41 (Figure 2a), the number of stars increases toward fainter magnitudes until $V = 20$ mag, beyond which there is a sharp decline. A similar trend is observed for NGC 1342 (Figure 2c), where the decrease in star counts begins at $V = 19$ mag. However, the star counts at $V = 19$ and 20 mag are found to be comparable. Consequently, the photometric completeness limit in the *UBV* system was adopted as $V = 20$ mag for both clusters. Similarly, panels (b) and (d) of Figure 2 depict the distributions

of star counts in G magnitudes with 0.5 mag bins for Czernik 41 and NGC 1342, respectively. The magnitudes at which the star counts reach their highest values are identified as $G = 21$ mag for Czernik 41 (Figure 2b) and $G = 21$ mag for NGC 1342 (Figure 2d).

To check the photometric completeness limits, we generated synthetic star populations for the regions of both OCs using the Besançon Galaxy Model⁵ (Robin et al. 2003, 2012). This model incorporates the three-dimensional interstellar medium extinction map developed by Marshall et al. (2006), enabling a realistic representation of extinction along different lines of sight. The simulations were performed within the magnitude intervals of $10 < V$ (mag) ≤ 23 and $9 < G$ (mag) ≤ 23 , consistent with the observational star counts and taking into account the three-dimensional extinction values from Marshall et al. (2006). Since the *UBV* and *Gaia* photometric data sets span different areas of the sky, solid angles of 0.1225 and 0.4450 square degrees, respectively, were adopted in the model.

The resulting synthetic star counts are presented alongside the observational data in Figure 2. The magnitude intervals in which the number of observed stars exceeds that of the model, particularly at the bright end of the V and G bands, represent the dominant magnitude ranges of the OCs (i.e., completeness is $\sim 100\%$). Conversely, the apparent magnitudes at which the model star counts begin to surpass the observed counts correspond to the photometric completeness limits. Therefore, we conclude that there is no loss of stars within the previously defined photometric completeness limits in this study.

The apparent magnitude and color index uncertainties of the stars detected in the cluster fields, derived

⁵ <https://model.obs-besancon.fr/>

from the *UBV* and *Gaia* photometric systems, are listed in Table 6 as a function of apparent magnitudes in *V* and *G*. The magnitude and color uncertainties were determined based on the statistical uncertainties in instrumental magnitudes and the propagation of errors in the corresponding bands. For Czernik 41, considering the photometric completeness limit in the *V* band, the mean uncertainties in apparent magnitudes within the range $9 < V \text{ (mag)} \leq 20$ were found to be no greater than 0.05 mag for *V*, and 0.16 mag for the *U*–*B* and *B*–*V* color indices. For NGC 1342, in the range $8 < V \text{ (mag)} \leq 20$, the mean uncertainties were even smaller, not exceeding 0.025 mag for *V*, and 0.05 mag for the *U*–*B* and *B*–*V* color indices. An examination of the mean uncertainties in *Gaia* photometry showed that for $5 < G \text{ (mag)} \leq 21$ in Czernik 41 and $7 < G \text{ (mag)} \leq 21$ in NGC 1342, the mean uncertainties in *G* magnitudes were no greater than 0.007 mag, while the uncertainties in the $G_{\text{BP}} - G_{\text{RP}}$ color indices did not exceed 0.16 mag.

3.2. The Radial Density Profile

Gaia photometric data were utilized in the radial density profile (RDP) analysis of both OCs. The photometric *G* magnitudes of stars were considered to calculate the structural parameters from the RDP. Stellar number density profiles were subsequently generated. The central coordinates of the OCs in the equatorial coordinate system were taken from the catalog of Cantat-Gaudin et al. (2020). In the analysis, stars within concentric annuli of varying radii, defined from the cluster center, were initially counted. The stellar number density for each annulus was then computed by dividing the number of stars by the area of the annulus (i.e., $\rho(r_i) = N_i/A_i$; N and A represent the number of stars in the defined annulus and the area of the annulus, respectively, with the index i denoting the corresponding annulus). RDPs were constructed as a function of distance from the cluster center and compared with the King (1962) model which is described as $\rho(r) = f_{\text{bg}} + [f_0/(1 + (r/r_c)^2)]$ (where r , f_0 , r_c , and f_{bg} represent the radius from the cluster centre, the central density, core radius, and background density, respectively). To derive the best-fitting model, a χ^2 minimization method was applied to the RDPs. The final parameter estimates were determined as the values that minimized the computed χ^2 . The resulting RDPs for Czernik 41 and NGC 1342, along with the best-fit King (1962) models, are presented in Figure 3. The structural parameters derived from these models follow as the central stellar density (f_0), core radius (r_c), and background stellar density (f_{bg}) of both OCs were determined as follows: for Czernik 41,

Table 5. The catalogs for Czernik 41 and NGC 1342. The complete table can be found electronically.

Czernik 41													NGC 1342												
ID	RA (hh:mm:ss.ss)	DEC (dd:mm:ss.ss)	V (mag)	U–B (mag)	B–V (mag)	G (mag)	$G_{\text{BP}} - G_{\text{RP}}$ (mag)	$\mu_{\alpha} \cos \delta$ (mas yr ⁻¹)	μ_{δ} (mas yr ⁻¹)	ϖ (mas)	P	ID	RA (hh:mm:ss.ss)	DEC (dd:mm:ss.ss)	V (mag)	U–B (mag)	B–V (mag)	G (mag)	$G_{\text{BP}} - G_{\text{RP}}$ (mag)	$\mu_{\alpha} \cos \delta$ (mas yr ⁻¹)	μ_{δ} (mas yr ⁻¹)	ϖ (mas)	P		
0001	19:50:14.48	+25:08:58.48	15.114(0.014)	0.695(0.041)	1.098(0.020)	14.931(0.003)	1.241(0.005)	-5.555(0.022)	2.968(0.014)	1.662(0.023)	0.000	001	03:30:46.83	+37:27:21.01	19.013(0.023)	—	1.879(0.058)	18.543(0.007)	2.413(0.046)	-6.62(0.323)	4.979(0.420)	0.032(0.364)	0.162		
0002	19:50:14.54	+25:10:44.54	18.013(0.011)	0.406(0.054)	1.378(0.019)	17.504(0.003)	1.896(0.011)	-0.043(0.078)	1.373(0.052)	0.460(0.079)	0.090	002	03:30:46.93	+37:28:24.89	18.882(0.013)	—	1.060(0.021)	18.538(0.003)	1.371(0.036)	-2.166(0.188)	2.457(0.235)	0.077(0.220)	0.209		
0003	19:50:14.66	+25:12:55.64	16.593(0.042)	—	1.489(0.067)	16.003(0.003)	1.863(0.006)	6.217(0.037)	4.404(0.024)	0.835(0.037)	0.448	003	03:30:47.03	+37:23:37.49	15.557(0.002)	0.618(0.006)	1.114(0.003)	15.096(0.003)	1.538(0.005)	-5.353(0.036)	6.682(0.041)	0.642(0.032)	0.000		
0004	19:50:15.03	+25:12:03.83	19.067(0.027)	—	1.620(0.053)	18.382(0.003)	2.087(0.027)	-11.576(0.134)	-0.643(0.088)	0.504(0.134)	0.000	004	03:30:47.15	+37:27:57.87	17.085(0.004)	0.497(0.014)	1.013(0.006)	16.774(0.003)	1.318(0.008)	0.218(0.064)	2.006(0.079)	0.285(0.073)	0.000		
...		
2524	19:51:44.80	+25:23:42.50	18.562(0.016)	—	1.650(0.031)	18.219(0.003)	2.019(0.027)	—	1.117(0.208)	-9.733(0.116)	0.251	903	03:32:29.39	+37:24:00.47	15.988(0.002)	1.039(0.011)	1.367(0.004)	15.43(0.003)	1.719(0.006)	1.099(0.035)	16.948(0.046)	0.727(0.041)	0.000		
2525	19:51:44.88	+25:23:13.43	16.053(0.027)	—	1.296(0.041)	15.712(0.003)	1.531(0.005)	—	0.734(0.313)	7.504(0.029)	0.000	904	03:32:29.82	+37:30:03.34	18.117(0.008)	—	1.778(0.017)	17.185(0.003)	2.208(0.016)	-2.082(0.088)	-0.059(0.105)	1.621(0.095)	0.310		
2526	19:51:45.13	+25:25:01.08	18.223(0.013)	—	1.720(0.026)	17.399(0.003)	2.268(0.010)	—	1.602(0.553)	-4.235(0.071)	0.298	905	03:32:30.05	+37:24:07.67	19.024(0.014)	—	1.026(0.023)	18.600(0.003)	1.443(0.049)	-0.945(0.204)	-0.892(0.261)	0.430(0.239)	0.000		
2527	19:51:45.16	+25:26:53.32	17.462(0.007)	—	1.745(0.015)	16.611(0.003)	2.291(0.007)	—	0.701(0.212)	-5.339(0.043)	0.235	906	03:32:30.30	+37:32:04.81	19.448(0.023)	—	2.101(0.063)	19.449(0.004)	—	1.191(0.973)	11.215(0.856)	3.434(0.522)	0.000		

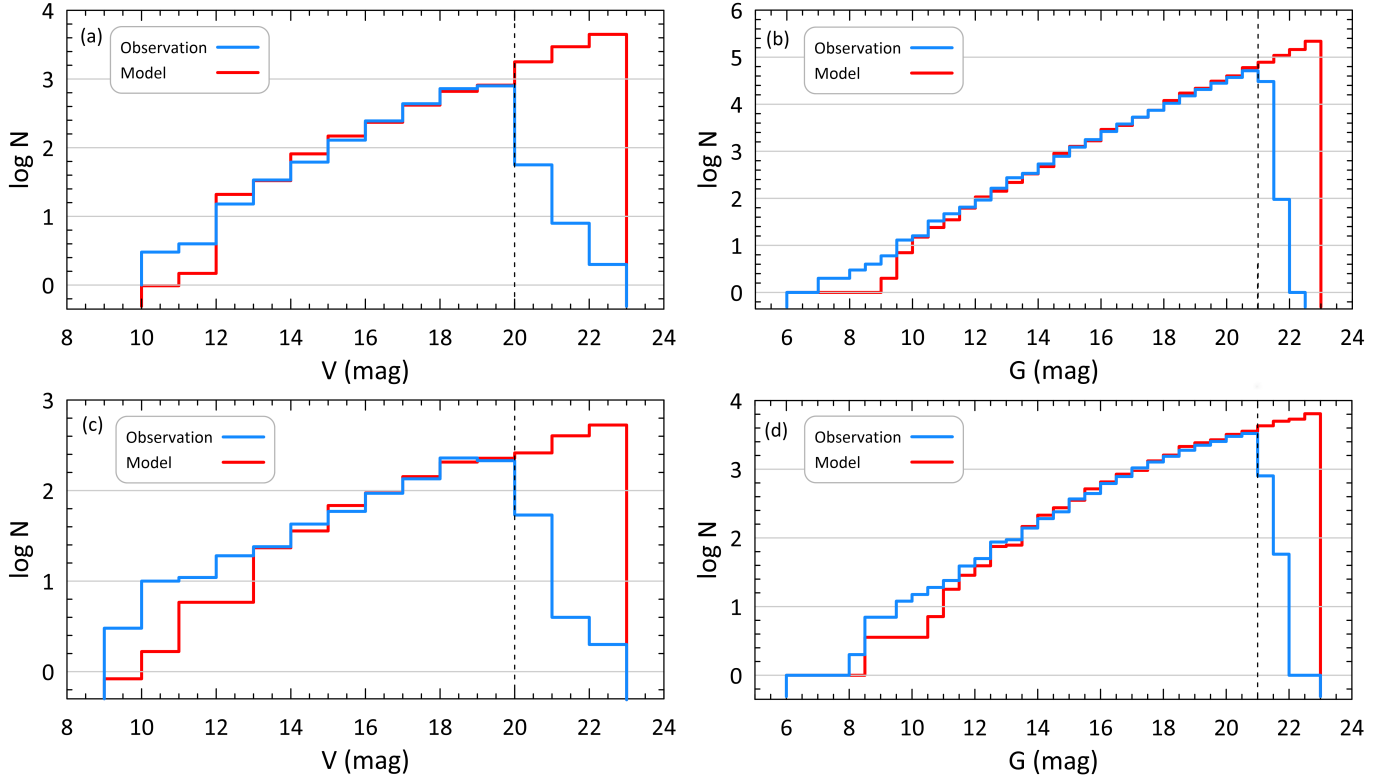


Figure 2. Histograms of stars in Czernik 41 (panels a and b) and NGC 1342 (panels c and d) as a function of V and G magnitudes. The black dashed lines show the photometric completeness limits for each band. The blue and red color bins represent the observed and the Besançon Galaxy model values, respectively.

$f_0 = 7.622 \pm 0.750$ stars arcmin $^{-2}$, $r_c = 1.728 \pm 0.266$ arcmin, and $f_{bg} = 4.481 \pm 0.171$ stars arcmin $^{-2}$, while for NGC 1342, these values were found to be $f_0 = 1.733 \pm 0.240$ stars arcmin $^{-2}$, $r_c = 2.155 \pm 0.568$ arcmin, and $f_{bg} = 1.766 \pm 0.090$ stars arcmin $^{-2}$. As shown in Figure 3, the background density, represented by the horizontal grey band, intersects the RDP model at the limiting radius for two clusters. Consequently, the limiting radius for both OCs was assumed as $r_{lim} = 11'$. In the subsequent analyses, only stars within these limiting radii were considered, while stars located beyond the limiting radius, where field stars dominate, were excluded from the following statistical analysis of the clusters' fundamental parameters.

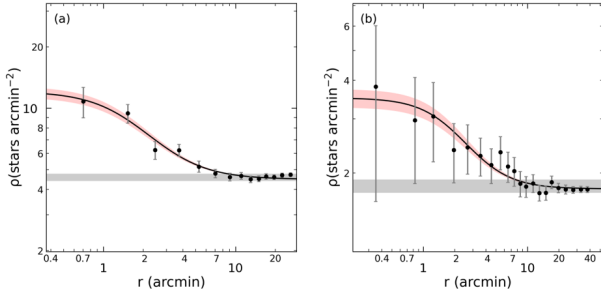
The concentration parameter of a cluster is an indicator for understanding its internal structure and evolutionary process, reflecting the combined effects of formation mechanisms, dynamical interactions, and environmental influences within the Galaxy. In general, the concentration parameter is defined using the limiting radius (r_{lim}) instead of the tidal radius (r_{tidal}) as in the classical King model definition, $C = \log(r_{tidal}/r_{core})$. We acknowledge that these two radii are conceptually distinct; however, in practice, they are often found to be closely related, particularly in systems where the tidal

cutoff is not sharply defined or cannot be robustly constrained observationally. Several previous studies have adopted a similar approach, using r_{lim} as a proxy for r_{tidal} due to observational limitations and the practical difficulties in distinguishing between the two radii in low-surface-brightness systems. For example, Hill & Zaritsky (2006) and Muñoz et al. (2010) employed limiting radii derived from surface brightness or star count profiles as effective substitutes for the formal tidal radius in their structural analyses of dwarf galaxies. Likewise, Miocchi et al. (2013) discussed that for globular clusters, particularly those with extended halos, the limiting radius obtained from observational profiles can serve as a reasonable approximation of the tidal radius.

In this study, C values were determined as 0.804 ± 0.062 and 0.708 ± 0.102 for Czernik 41 and NGC 1342, respectively. The derived concentration parameters for both OCs are relatively low, indicating a mild stellar density gradient between the core and the outer regions. This reflects a weak central concentration, suggesting that the clusters exhibit structural characteristics typical of dynamically unevolved or loosely bound systems. The effect of mass segregation in these clusters is expected to be weaker as the migration of more massive stars toward the center has not yet fully progressed.

Table 6. Mean internal photometric uncertainties for each magnitude bin in V and G magnitudes.

Czernik 41					NGC 1342			
V	N	σ_V	σ_{U-B}	σ_{B-V}	N	σ_V	σ_{U-B}	σ_{B-V}
[08, 12]	10	0.002	0.003	0.003	26	0.001	0.003	0.002
(12, 14]	49	0.007	0.014	0.011	43	0.004	0.009	0.006
(14, 15]	62	0.011	0.036	0.017	43	0.004	0.011	0.006
(15, 16]	129	0.016	0.070	0.031	59	0.002	0.013	0.005
(16, 17]	249	0.019	0.106	0.023	94	0.003	0.014	0.013
(17, 18]	436	0.023	0.137	0.046	135	0.006	0.025	0.026
(18, 19]	725	0.032	0.155	0.058	231	0.012	0.037	0.045
(19, 20]	801	0.044	0.162	0.125	215	0.024	0.052	0.057
(20, 22]	66	0.057	0.193	0.168	60	0.034	0.069	0.065
G	N	σ_G	$\sigma_{G_{BP}-G_{RP}}$	N	σ_G	$\sigma_{G_{BP}-G_{RP}}$		
[06, 12]	6	0.003	0.006	34	0.003	0.005		
(12, 14]	46	0.003	0.006	104	0.003	0.005		
(14, 15]	84	0.003	0.007	82	0.003	0.005		
(15, 16]	228	0.003	0.012	147	0.003	0.006		
(16, 17]	566	0.003	0.014	212	0.003	0.009		
(17, 18]	1334	0.003	0.025	354	0.003	0.019		
(18, 19]	2703	0.003	0.052	581	0.003	0.042		
(19, 20]	5121	0.004	0.094	770	0.004	0.082		
(20, 23]	5881	0.006	0.154	475	0.007	0.157		

**Figure 3.** King profiles of Czernik 41 (a) and NGC 1342 (b). The black solid curves represent the best-fit models, while the shaded red and grey regions indicate the confidence intervals of the model and the background stellar density, respectively. The dashed vertical lines denote the limit radii of the OCs.

Consequently, clusters with low concentration parameters may be dynamically young or may have lost their central density over time due to external influences (Elson et al. 1987).

3.3. CMDs and Cluster Membership

The membership probabilities of stars within the fields of the OCs studied in this study were calculated using the UPMASK method (Krone-Martins & Moitinho

2014). The *Gaia* DR3 (Gaia Collaboration et al. 2023) catalogs created for Czernik 41 and NGC 1342 were utilized, employing a five-dimensional parameter space comprising positional and astrometric data to compute the membership probabilities of stars. Specifically, the input parameters for the program included the equatorial coordinates (α , δ), trigonometric parallaxes (ϖ), PM components ($\mu_\alpha \cos \delta$, μ_δ), and their associated uncertainties for each star in the catalogs. UPMASK was run with k -means values ranging from 6 to 30 and 25 iterations. The optimal k -means values were selected based on the configurations that best represented the cluster structure through the computed membership probabilities. Consequently, the k -means values for Czernik 41 and NGC 1342 were set to 8 and 25, respectively.

Color-magnitude diagrams (CMDs) serve as a fundamental tool for revealing the relationship between magnitude and color, thereby enabling the determination of the age, mass, and evolutionary status of member stars in OCs. Moreover, CMDs play a crucial role in testing stellar evolution models and deriving cluster parameter estimates with high precision. As discussed above, in this study stars located in the direction of the clusters were analyzed using *Gaia* DR3 astrometric data, leading to high-probability members being selected via the UPMASK algorithm. The morphological features observed in the CMDs are essential for deriving key astrophysical parameters such as color excess, distance, and age of the OCs. Therefore, isochrone fitting based on a sample composed exclusively of stars with reliable membership probabilities allows for a more accurate determination of these parameters. We note that unresolved binary systems may cause a noticeable broadening in the CMD, complicating the interpretation of the stellar distribution. To better assess this effect and to improve the accuracy of the derived cluster parameters, high-probability member stars were plotted on CMDs constructed using both UBV and *Gaia* photometric magnitude and colors. Based on the *Gaia* data, stars within the cluster direction satisfying the conditions of limiting magnitude ($G \leq 21$), membership probability ($P \geq 0.5$), and limiting radius ($r_{\text{lim}} = 11'$) were identified and shown in the $G \times (G_{BP} - G_{RP})$ CMDs. Under these criteria, 382 stars were identified as members of Czernik 41, and 111 stars as members of NGC 1342. Stars selected based on the specified criteria are presented in Figure 4 on the $G \times (G_{BP} - G_{RP})$ CMDs as a function of their membership probabilities.

In the UBV photometric system, a consistent method was employed to ensure uniformity in the determination of cluster structure. Following the *Gaia*-based ap-

proach, the lower boundary of the cluster main sequence was again adjusted to account for photometric dispersion and unresolved binaries, but using a different reference. Instead of theoretical isochrones, the observational ZAMS from Sung et al. (2013) was applied to the $V \times (B - V)$ CMDs. The ZAMS curve was shifted empirically in both V and $B - V$ directions to encapsulate the combined effects of interstellar extinction, unresolved binary presence, and photometric uncertainties. This refinement allowed for the selection of probable main-sequence members and bright stars near the cluster turn-off point and giant regions with $P \geq 0.5$. By applying these photometric criteria, the member selection process was harmonized across the two photometric systems, improving the reliability of the cluster analysis. In conclusion, for the UBV system, the most probable members of the clusters were defined as stars within $r_{\text{lim}} \leq 11'$, with $V \leq 20$ mag, $P \geq 0.5$, and located within the ZAMS-constrained regions. The number of these stars is 172 for Czernik 41 and 89 for NGC 1342. These stars were subsequently utilized in determining the clusters' UBV -based parameter estimates. The distributions of stars identified in the UBV system in the $V \times (B - V)$ diagrams, along with the ZAMS-constrained bands, are shown in Figure 4a (Czernik 41) and Figure 4c (NGC 1342), where the continuous and dashed blue curves represent the ZAMS boundaries. Additionally, the $G \times (G_{\text{BP}} - G_{\text{RP}})$ diagrams for stars detected in the *Gaia* data are displayed in Figure 4b (Czernik 41) and Figure 4d (NGC 1342). In both the UBV - and *Gaia*-based diagrams, stars marked according to their color scale represent the most probable cluster members, which satisfy $r_{\text{lim}} \leq 11'$ and $P \geq 0.5$.

Figure 5 presents the probability histograms of stars identified in the cluster *Gaia*-based catalogs. These histograms include stars located within the limiting radii ($r_{\text{lim}} \leq 11'$) and that are brighter than the photometric G completeness limits. The analysis of stars with membership probabilities $P \geq 0.5$ within the limiting radii reveals that their proportions relative to all stars in the $40' \times 40'$ cluster field, spanning probabilities $0 \leq P \leq 1$, are 2.34% for Czernik 41 and 3.77% for NGC 1342. This shows that field contamination is very high, confirming that these are not strongly populated clusters.

The proper motion (PM) distributions of stars in the *Gaia* catalogs for the fields of Czernik 41 and NGC 1342, along with their vectorial motion directions in equatorial coordinates, are presented in Figure 6. An examination of the PM diagrams for the most probable cluster members (colored circles) reveals that the open clusters Czernik 41 (Figure 6a) and NGC 1342 (Figure 6c) are embedded within the field stars (gray

circles). However, it is evident that stars with membership probabilities $P \geq 0.5$ are clustered within specific regions, with Czernik 41 containing a denser stellar population compared to NGC 1342. In panels of Figures 6b and d, the most probable member stars (represented by colored arrows) exhibit a consistent vectorial alignment across the sky. The mean PM components $\langle \mu_{\alpha} \cos \delta, \mu_{\delta} \rangle$ derived from the most probable member stars of Czernik 41 and NGC 1342 are calculated as $(-2.963 \pm 0.068, -6.163 \pm 0.101)$ mas yr $^{-1}$ and $(0.419 \pm 0.041, -1.662 \pm 0.031)$ mas yr $^{-1}$, respectively. In Figures 6a (Czernik 41) and c (NGC 1342), the intersections of the dashed blue lines indicate the mean PM values of the OCs.

The mean trigonometric parallaxes $\langle \varpi \rangle$ of the clusters were determined by fitting Gaussian functions to the parallax histograms of the most probable cluster members. To ensure precise measurements, a relative parallax error constraint of $\sigma_{\varpi}/\varpi < 0.2$ was applied. Based on this, the $\langle \varpi \rangle$ of Czernik 41 and NGC 1342 were calculated as 0.381 ± 0.048 mas and 1.523 ± 0.051 mas, respectively. The parallax histograms and Gaussian fit for both clusters are shown in Figure 7. Using the linear relation $d_{\varpi}(\text{pc}) = 1000/\varpi(\text{mas})$, the distances were derived as 2625 ± 331 pc for Czernik 41 and 657 ± 22 pc for NGC 1342.

4. ASTROPHYSICAL PARAMETERS OF THE CLUSTERS

This section provides a summary of the methodologies employed in the astrophysical analysis of the star clusters Czernik 41 and NGC 1342. The reddening and photometric metallicities were independently estimated using two-color diagrams (TCDs). With these parameters held constant, the distance moduli and ages of the clusters were simultaneously derived from the CMDs. For a comprehensive explanation of the methodology, see the studies as follows Yontan et al. (2023b); Bilir et al. (2016); Bostancı et al. (2018).

4.1. UBV Based Color Excesses

The color excesses $E(B - V)$ and $E(U - B)$ for Czernik 41 and NGC 1342 were determined using the $(U - B \times B - V)$ TCDs. Initially, member stars with probabilities $P \geq 0.5$ within the defined limiting radii were selected, leading to the construction of $(U - B \times B - V)$ TCDs for both OCs. For Czernik 41, 27 stars within the apparent magnitude range of $14 \leq V$ (mag) ≤ 17 were identified, and for NGC 1342, 56 stars within the range $12 \leq V$ (mag) ≤ 19 were selected. The solar metallicity ZAMS of Sung et al. (2013) was shifted iteratively until it best matched the stars

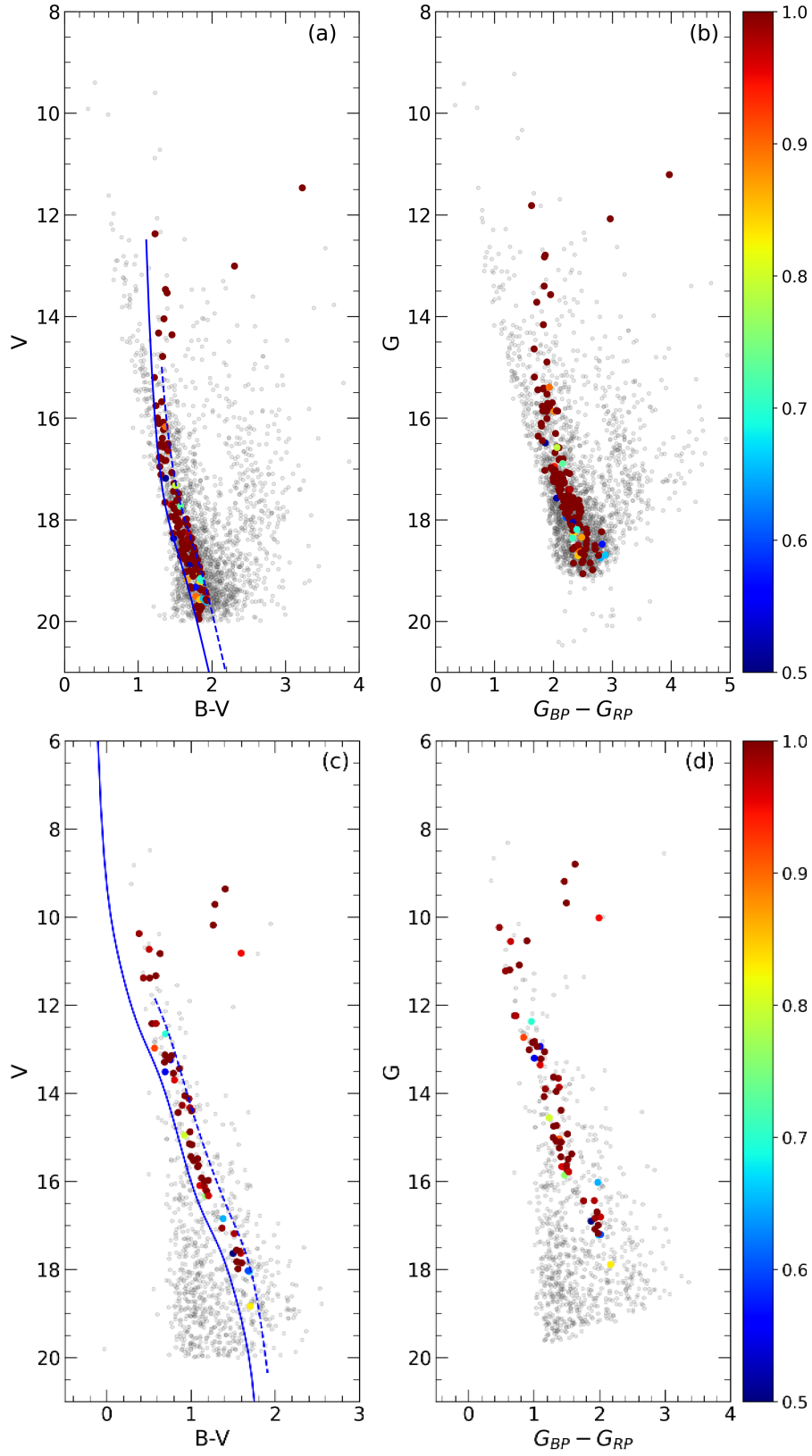


Figure 4. CMDs of Czernik 41 (a-b) and NGC 1342 (c-d) in the *UBV* (a and c) and *Gaia* (b and d) photometric systems. Gray circles represent stars with membership probabilities $P < 0.5$, while colored circles indicate stars with $P \geq 0.5$. The continuous and dashed blue curves denote the ZAMS lines used to define the cluster main sequences (Sung et al. 2013).

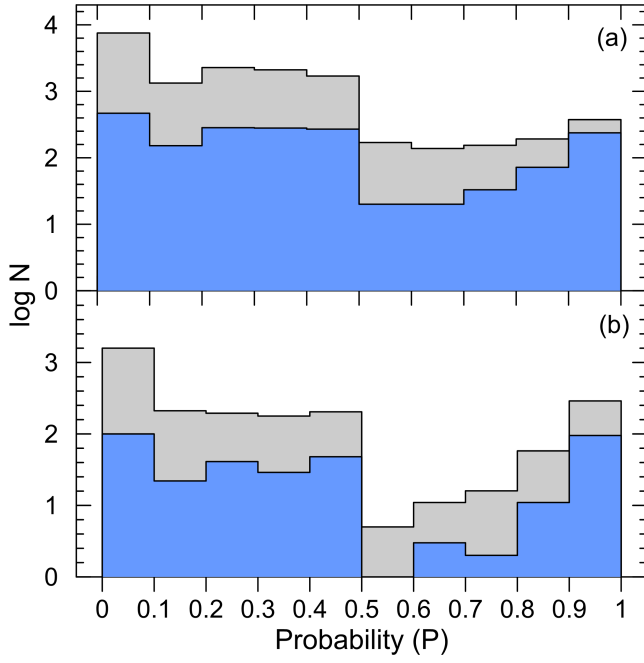


Figure 5. Membership probability distributions for all stars detected in the cluster fields of Czernik 41 (a) and NGC 1342 (b), constructed for *Gaia* data. The filled grey histograms represent the membership probabilities of all stars identified within the cluster fields, while the filled blue histograms correspond to stars within the limit radius ($r_{\text{lim}} \leq 11'$).

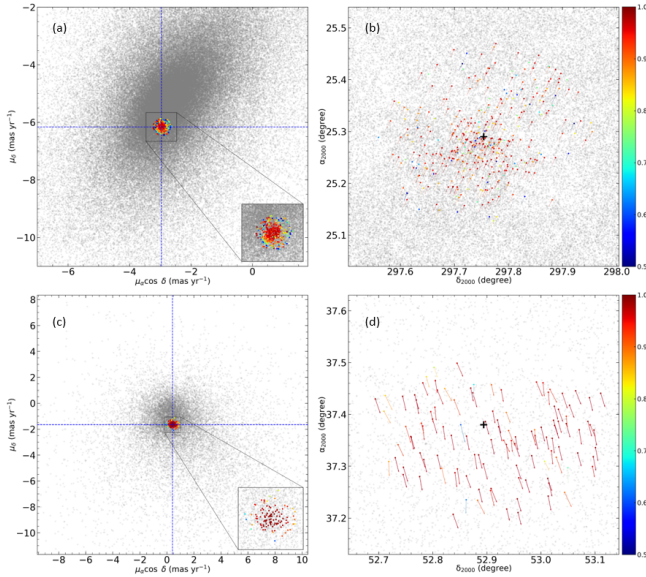


Figure 6. Czernik 41 (a-b) and NGC 1342 (c-d) OC fields: *Gaia* DR3 PM components (left panels) and sky orientation vectors in equatorial coordinates (right panels). The color scale and circles are identical to Figure 4. Black plus signs in panels (b) and (d) denote the central equatorial coordinates of the OCs.

marked on the $(U-B \times B-V)$ TCDs. To compare the re-

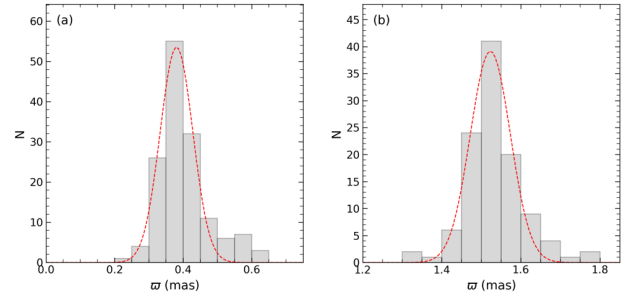


Figure 7. Trigonometric parallax histograms for the members of Czernik 41 (a) and NGC 1342 (b) within the limiting radius ($r_{\text{lim}} \leq 11'$) and with a relative parallax error of $\sigma_{\pi}/\pi < 0.2$. The Gaussian functions applied to the distributions are shown as dashed red lines.

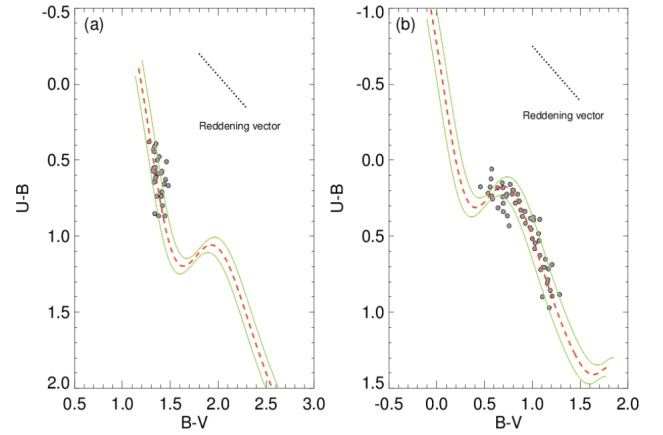


Figure 8. The TCDs of the most probable main-sequence stars in the regions of the OCs Czernik 41 (a) and NGC 1342 (b) are presented. The reddened ZAMS, as defined by Sung et al. (2013), is depicted by the red dashed curves, while the green solid curves indicate the $\pm 1\sigma$ standard deviations.

sults, the color excesses were calculated using the equation $E(U-B)/E(B-V) = 0.72 + 0.05 \times E(B-V)$ (Garcia et al. 1988) over the range $0 < E(B-V)$ (mag) < 2 , with steps of 0.01 mag. A χ^2 minimization was applied, with the color excesses corresponding to the minimum χ^2 value being accepted as the best fit. The derived color excess values for both OCs are as follows: for Czernik 41, $E(B-V) = 1.500 \pm 0.035$ mag and $E(U-B) = 1.080 \pm 0.025$ mag, and for NGC 1342, $E(B-V) = 0.270 \pm 0.043$ mag and $E(U-B) = 0.194 \pm 0.031$ mag. The ZAMS curves, which best fit the members of main-sequence stars in the $(U-B \times B-V)$ TCDs, are shown in Figure 8 as red dashed lines. The uncertainties in the color excesses, corresponding to one standard deviation (1σ), are indicated by green solid lines.

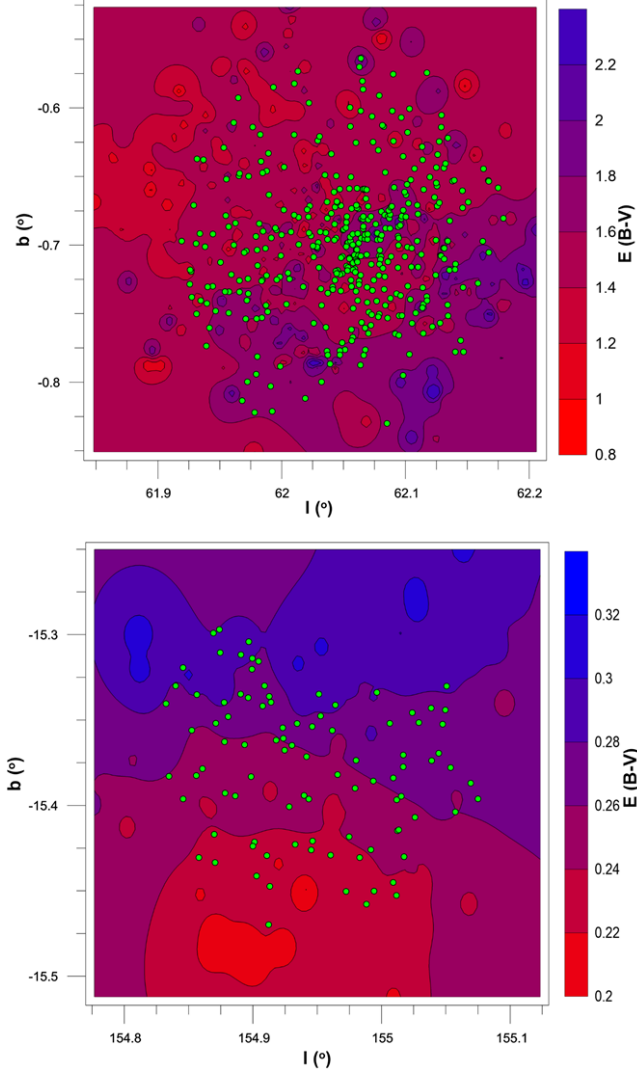


Figure 9. The spatial distributions of member stars in Czernik 42 (top) and NGC 1342 (bottom) are presented in Galactic coordinates (l, b) . Contour lines were generated based on color excess values derived from dust maps. The color scale in the right-hand panels indicates the magnitude of the color excess corresponding to the contour levels.

We used the [Schlafly & Finkbeiner \(2011\)](#) dust maps to check the reliability of the color excesses calculated for the clusters and also to assess the possibility of differential reddening within the OCs. Based on these maps and the equatorial coordinates of stars with high membership probabilities, we obtained V -band extinctions up to the Galactic edge. These V -band extinction values were then scaled to star-Sun distances using the relation given by [Bahcall & Soneira \(1980\)](#):

$$A_d(V) = A_\infty(V) \times \left[1 - \exp\left(\frac{-|d \times \sin b|}{H}\right) \right] \quad (2)$$

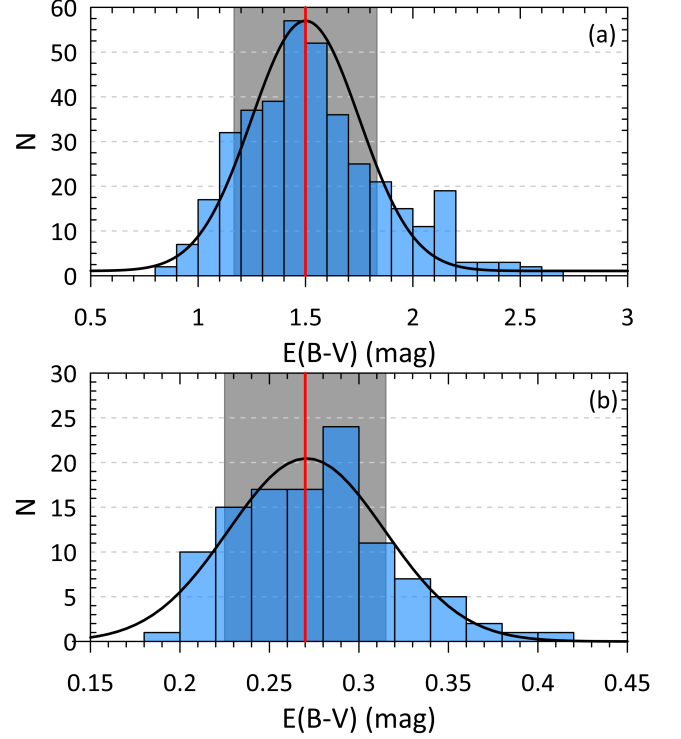


Figure 10. Color excess histograms for the (a) Czernik 41 and (b) NGC 1342 OCs, estimated using the 3D-dust maps and distances between the Sun and individual stars calculated from trigonometric parallax data. The red line represents the mean color excess, while the gray-shaded area indicates the $\pm 1\sigma$ standard deviation range.

b represents the Galactic latitude of the star while d denotes its distance, determined using the trigonometric parallax measurements from the *Gaia* DR3 catalog via the relation $d(\text{pc}) = 1000/\varpi$ (mas). The parameter H corresponds to the dust scale height ($H = 125^{+17}_{-7}$ pc, [Marshall et al. 2006](#)). $A_\infty(V)$ represents the V -band extinction integrated along the line of sight to the Galactic boundary. The extinction value corresponding to the distance between the Sun and a star is given by $A_d(V)$. The relation $E_d(B - V) = 3.1 \times A_d(V)$ was used to convert the calculated reduced V -band extinctions into reduced color excess.

Figure 9 illustrates the spatial distribution of cluster member stars, color-coded according to their color excess values. The analysis reveals that the color excess values range from 0.8 to 2.4 mag for Czernik 41 and from 0.2 to 0.34 mag for NGC 1342. Figure 10 presents the histograms of the color excess distributions for the cluster members. Statistical analysis yields skewness values of 0.648 for Czernik 41 and 0.521 for NGC 1342, indicating a moderate positive skewness in the color excess distributions of both clusters. By fitting Gaussian curves to the distributions, the mean color excesses and cor-

responding standard deviations were determined to be (1.50, 0.33) mag for Czernik 41 and (0.27, 0.04) mag for NGC 1342. As can be seen in Figure 9, Czernik 41 exhibits clear evidence of differential reddening, although the majority of the cluster members are concentrated around the median color excess value. In contrast, NGC 1342 shows a lower level of differential reddening, suggesting a more homogeneous distribution of interstellar extinction across the cluster.

4.2. Photometric Metallicity

The photometric metallicity calibration developed by Karaali et al. (2011), which is sensitive to ultraviolet (UV) excess for F-G spectral type main-sequence stars, was employed to determine the metallicities ($[\text{Fe}/\text{H}]$) of the OCs. Through considering the calculated color excesses of the OCs, the intrinsic color indices $(U - B)_0$ and $(B - V)_0$ of the member stars were derived. F-G type main-sequence stars within the color range $0.3 \leq (B - V)_0$ (mag) ≤ 0.6 , with membership probabilities $P \geq 0.5$, and located within the limit radii ($r_{\text{lim}} \leq 11'$) of the OCs, were selected for the metallicity estimation (Eker et al. 2018, 2020; Eker et al. 2024; Eker & Bakış 2025). Since no *UBV* photometry was obtained for main-sequence stars in Czernik 41, there is no estimate of the metallicity from the two-color diagram for this cluster, whereas for NGC 1342, the photometric metallicity was determined using nine main-sequence stars satisfying the selection criteria. A $(U - B)_0 \times (B - V)_0$ TCD was constructed for these stars, and their data were compared with the Hyades main sequence to compute UV-excess values. The UV-excess, defined as $\delta = (U - B)_{0,\text{H}} - (U - B)_{0,\text{S}}$, represents the difference in $(U - B)_0$ indices, where the subscripts H and S refer to the Hyades and cluster stars, respectively. Following the approach described in Karaali et al. (2011), we normalized the UV-excess values to $(B - V)_0 = 0.6$ mag, obtaining $\delta_{0.6}$. The mean $\delta_{0.6}$ was determined by fitting a Gaussian function to the histogram of $\delta_{0.6}$ (Karaali et al. 2003b,a). The peak of each Gaussian fit provided the mean $\delta_{0.6}$ value, which was found to be $\delta_{0.6} = 0.056 \pm 0.014$ mag for NGC 1342. The uncertainties reflect the standard deviation $\pm 1\sigma$ of the Gaussian fits. The photometric metallicity of NGC 1342 was calculated using the calibration equation of $[\text{Fe}/\text{H}] = -14.316 \times \delta_{0.6}^2 - 3.557 \times \delta_{0.6} + 0.105$ presented by Karaali et al. (2011). The $(U - B)_0 \times (B - V)_0$ TCD and the $\delta_{0.6}$ histograms for the selected stars in NGC 1342 are shown in Figure 11. The estimated photometric metallicity value for the cluster is $[\text{Fe}/\text{H}] = -0.14 \pm 0.07$ dex. Within the scope of the Large Sky Area Multi-Object Fiber Spectroscopic Telescope (LAMOST; Cui

et al. 2012; Deng et al. 2012; Zhao et al. 2012) spectroscopic sky survey, atmospheric parameters were derived for two stars in NGC 1342, each with a cluster membership probability of $P \geq 0.8$ (Fu et al. 2022). The spectroscopic analyses yielded a mean $[\text{Fe}/\text{H}]$ of -0.15 dex, which is consistent with the calculated cluster $[\text{Fe}/\text{H}]$. In this study, a photometric metallicity value based on UV-excess was determined to be -0.14 ± 0.07 dex, in good agreement with the LAMOST results.

To incorporate the effects of metallicity into the age determination, the heavy-element abundance (Z) of a given OC was derived using equations provided by Bovy⁶, which are developed for PARSEC isochrones (Bressan et al. 2012). The relevant equations are:

$$Z_x = 10^{[\text{Fe}/\text{H}] + \log(Z_\odot / (1 - 0.248 - 2.78 \times Z_\odot))} \quad (3)$$

and

$$Z = \frac{(Z_x - 0.2485 \times Z_x)}{(2.78 \times Z_x + 1)}. \quad (4)$$

Here, Z_x is an intermediate processing function. Z_\odot represents the solar heavy-element abundance, with a value of 0.0152. Z is a function of Z_x and is considered in determining the heavy element abundance of the cluster. For NGC 1342, the value Z was calculated as 0.012, whereas for Czernik 41, Z was assumed to be the value estimated from the method explained in Section 4.3.1.

4.3. Astrophysical Parameters for Czernik 41 and NGC 1342

To minimize parameter degeneracy during the determination of distance and age, the color excess and metallicity were independently derived using the *UBV* photometric system (see Sections 4.1 and 4.2) as the ‘classic method’, where parameters are determined separately. These parameters were then held constant, allowing for the simultaneous determination of the distance modulus and age. In contrast, within the *Gaia* photometric system, all astrophysical parameters were derived simultaneously by utilizing a Markov-Chain Monte Carlo (MCMC) approach. All approaches were conducted using the stars with a membership probability $P \geq 0.5$ and located within the cluster’s limiting radius ($r_{\text{lim}} \leq 11'$). The numbers of stars so determined are 172 for Czernik 41 and 89 for NGC 1342 in the *UBV*-based analysis, while for the MCMC approach, they are 382 and 111, respectively.

4.3.1. Parameter Estimation with Markov-Chain Monte Carlo

⁶ <https://github.com/jobovy/isodist/blob/master/isodist/Isochrone.py>

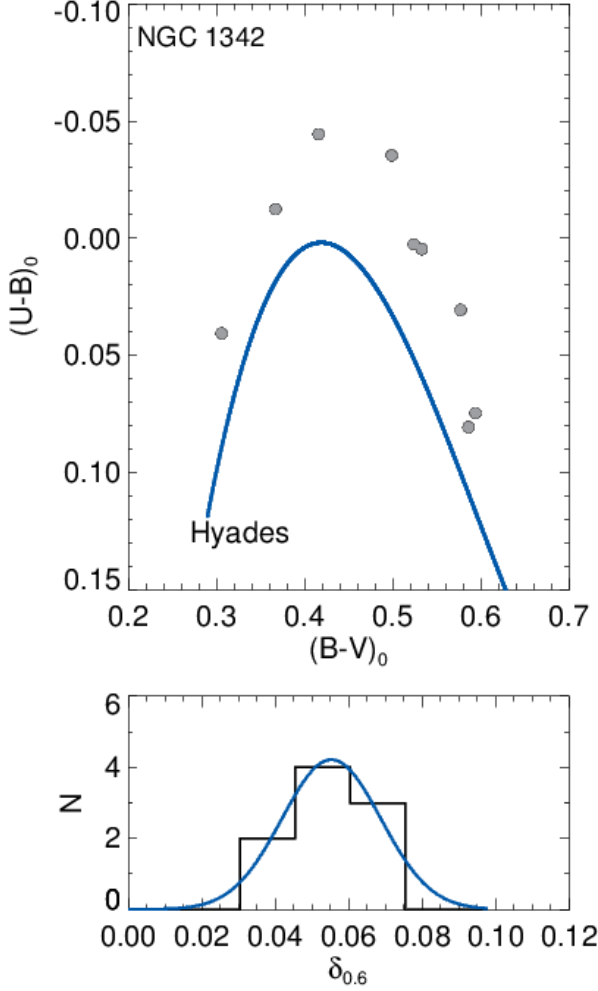


Figure 11. TCD for nine F-G type main-sequence stars ($P \geq 0.5$) in NGC 1342 is shown in the top panel. The blue curve in this panel represents the Hyades main sequence. The bottom panel illustrates the histogram of normalized UV-excesses ($\delta_{0.6}$), with a Gaussian function fitted to the distribution, depicted by the blue curve.

We developed a new method based on the Monte Carlo approach to independently determine the distance (d), extinction (A_G), age (τ), and metallicity (Z) of an OC. This method attempts to reach a common solution for the cluster by treating each member star as an independent ‘walker’ (or chain) over a specific isochrone grid. The grid used for this method was derived from version CMD 3.8⁷ of the PARSEC stellar isochrone library (Bressan et al. 2012). The properties of the obtained grid are as follows: in the $\log \tau$ space, steps of 0.05 were employed within the range of $6 \leq \log \tau$ (yr) ≤ 10.13 , while

⁷ <http://stev.oapd.inaf.it/cgi-bin/cmd>

Table 7. Fundamental parameters of the Czernik 41 and NGC 1342 derived using the MCMC for *Gaia* DR3 data.

	Czernik 41	NGC 1342
Parameter	$G \times (G_{BP} - G_{RP})$	$G \times (G_{BP} - G_{RP})$
A_G (mag)	$3.70_{-0.55}^{+0.54}$	$0.54_{-0.22}^{+0.22}$
d (pc)	2594_{-158}^{+123}	645_{-40}^{+27}
Z	$0.0176_{-0.0025}^{+0.0050}$	$0.0126_{-0.0050}^{+0.0025}$
$\log t$ (yr)	$7.94_{-0.48}^{+0.36}$	$8.99_{-0.25}^{+0.16}$

in the metallicity space Z , an isochrone grid was created with steps of 0.0005 dex in the range of $0 \leq Z \leq 0.03$.

The input parameter space for the Monte Carlo sampling was set as follows:

- Distance (d) ranging from 0 to 30 kpc,
- Extinction (A_G) ranging from 0 to 10 magnitudes,
- Metallicity (Z) and age (τ) spanning the full extent of the isochrone grid.

To interpolate the intermediate points of this constructed grid, the Delaunay function from the Python *Scipy* library (Virtanen et al. 2020) was used. This function enables a continuous space within the input grid by performing three-dimensional interpolation among the desired parameters of the input space. As a result, the obtained solution is free from the uncertainties introduced by the step size of the input grid and provides the continuous space required for the Monte Carlo method.

The relationship between the fundamental stellar parameters and the observed magnitudes in the *Gaia* photometric system can be expressed as follows:

$$m_X = M_X(\tau, Z) + \mu + A_X. \quad (5)$$

where:

- m_X represents the observed magnitude in band X ($X \in \{G, G_{BP}, G_{RP}\}$),
- $M_X(\tau, Z)$ is the absolute magnitude interpolated from the isochrone grid,
- $\mu = 5 \log d - 5$ is the distance modulus,
- $A_X = k_X A_G$ is the extinction correction for band X , with extinction coefficients k_X .

Expanding for each photometric band:

$$G = M_G(\tau, Z) + 5 \log d - 5 + A_G \quad (6)$$

$$G_{BP} = M_{BP}(\tau, Z) + 5 \log d - 5 + k_{BP} A_G \quad (7)$$

$$G_{RP} = M_{RP}(\tau, Z) + 5 \log d - 5 + k_{RP} A_G \quad (8)$$

where $M_X(\tau, Z)$ values are interpolated from the isochrone grid using the Delaunay triangulation method to ensure a smooth parameter space. The extinction coefficients k_{BP} and k_{RP} are 1.2955, 0.7586, respectively. These values are obtained by using [Cardelli et al. \(1989\)](#) and [O'Donnell \(1994\)](#) extinction curve with $R_V=3.1$.

The method aims to fit the observational data using a maximum likelihood approach by allowing each member star to act as a walker, traversing the input space while preserving the overall consistency. The likelihood function is:

$$\mathcal{L}(\theta) = \prod_{i=1}^{N_{\text{stars}}} \prod_{X \in \{G, G_{BP}, G_{RP}\}} P(m_{X,i}|\theta) \quad (9)$$

where $\theta = (\tau, Z, d, A_G)$ is the parameter set to be estimated. Assuming independent Gaussian errors, the probability distribution function is:

$$P(m_{X,i}|\theta) = \frac{1}{\sqrt{2\pi\sigma_{X,i}^2}} \exp\left(-\frac{(m_{X,i} - \hat{m}_{X,i})^2}{2\sigma_{X,i}^2}\right) \quad (10)$$

where $\hat{m}_{X,i}$ is the model-predicted magnitude:

$$\hat{m}_{X,i} = M_X(\tau, Z) + 5 \log d - 5 + A_X \quad (11)$$

and $\sigma_{X,i}$ is the observational uncertainty in band X . The log-likelihood function, which is more convenient for optimization, is:

$$\ln \mathcal{L}(\theta) = - \sum_{i=1}^{N_{\text{stars}}} \sum_X \left[\frac{(m_{X,i} - \hat{m}_{X,i})^2}{2\sigma_{X,i}^2} + \ln(\sqrt{2\pi}\sigma_{X,i}) \right] \quad (12)$$

A Monte Carlo sampling method is employed to explore the posterior distribution of the parameters. This method was implemented using the Python `emcee` library ([Foreman-Mackey et al. 2013](#)), a widely used affine-invariant MCMC sampler. Each cluster parameter is determined using as many walkers as the number of cluster members, with 5,000 iterations per walker. The final parameter estimates are obtained from the posterior distributions by taking the 16th, 50th, and 84th percentiles:

$$\theta_{\text{best}} = (Q_{50}(\theta), Q_{16}(\theta), Q_{84}(\theta)) \quad (13)$$

where $Q_p(\theta)$ represents the p -th percentile of the posterior distribution.

The method aims to ensure that the optimal solution for each star converges to the best solution for all stars, enabling the independent determination of the cluster's parameters. As a result of the analysis, the

ages, heavy-element abundances, distances, and extinction coefficients in the G band (A_G) for the two OCs were determined. The results are presented in [Table 7](#). [Figure 12](#) illustrates the posterior distributions for A_G , d , Z and $\log t$ derived for the two open clusters. The two-dimensional joint posterior distributions include contours that represent 68%, 90%, and 95% of the marginalized probability. In the one-dimensional marginalized distributions, vertical dashed lines indicate the 16th, 50th, and 84th percentiles, respectively. Using the parameters obtained from the MCMC analysis of *Gaia* data, CMDs were constructed, with the PARSEC model overlaid for validation. As illustrated in [Figures 13c and f](#), the estimated parameters show a strong agreement with the observed *Gaia*-based CMDs, demonstrating a high level of consistency between the data and the model.

[Bailer-Jones et al. \(2021\)](#) employed a Bayesian framework to infer the photogeometric distance from *Gaia* trigonometric parallaxes, incorporating interstellar extinction, color, and magnitude to construct posterior probability distributions. To associate individual cluster members with their corresponding entries in the [Bailer-Jones et al. \(2021\)](#) catalog, we performed a cross-matching procedure based on the equatorial coordinates of each cluster member, adopting a cross-match radius of less than 1 arcsec. Our analysis confirms that this choice of radius effectively minimizes the risk of multiple matches, even in relatively crowded cluster environments. After identifying the sources in the catalog, we constructed histograms of the photogeometric distance provided by [Bailer-Jones et al. \(2021\)](#). A Gaussian function was then fitted to these distributions to determine the median distances for two OCs. According to this analysis, the photogeometric distance for Czernik 41 is found to be $d_{\text{BJ21}} = 2575 \pm 322$ pc, while for NGC 1342, it is $d_{\text{BJ21}} = 646 \pm 17$.

4.3.2. Distance Moduli and Age Estimation

For the UBV -based analysis, the distance moduli (μ), distance (d), and ages (t) of Czernik 41 and NGC 1342 were determined using the PARSEC isochrones ([Bressan et al. 2012](#)). CMDs in $V \times (U - B)$, and $V \times (B - V)$ were constructed using stars identified in the cluster regions. Stars with a membership probability $P \geq 0.5$ and located within the cluster's limiting radius as $r_{\text{lim}} \leq 11'$ were highlighted on these CMDs. PARSEC isochrones, generated for a range of ages consistent with the heavy-element abundances (Z) of each cluster, were adjusted to match the observed CMDs. For Czernik 41, the Z value was adopted based on results obtained from an MCMC analysis (see [Table 7](#)), while for NGC 1342,

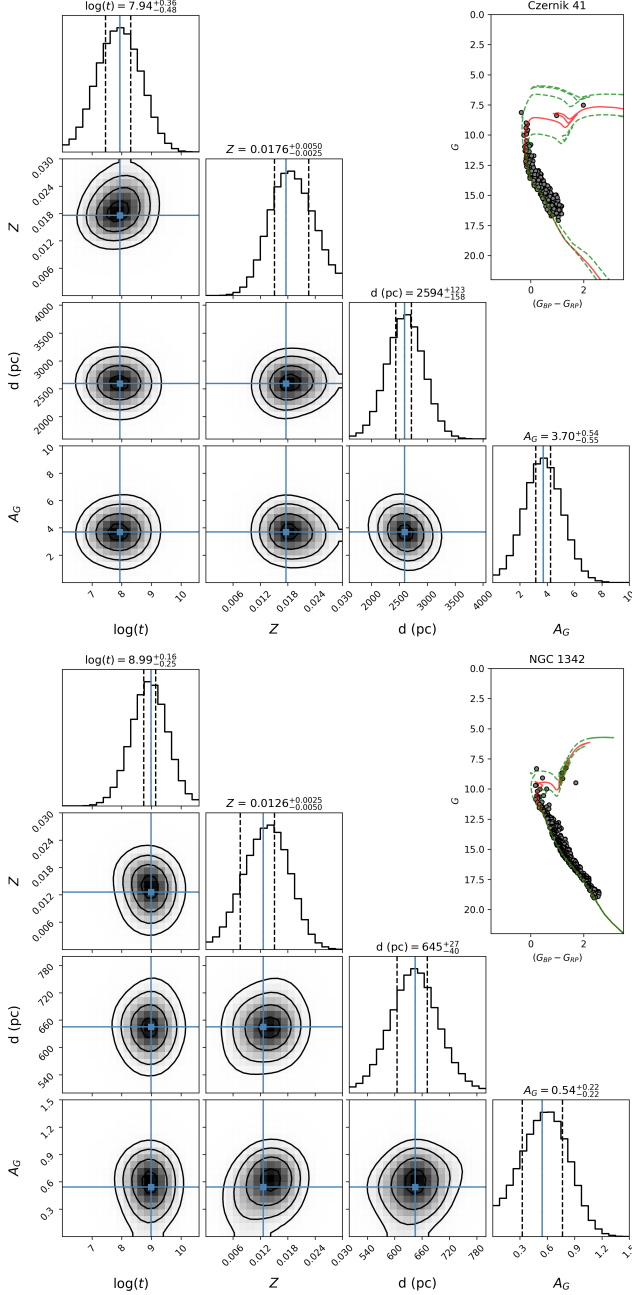


Figure 12. Corner plot illustrating the two-dimensional joint and one-dimensional marginalized posterior distributions for the properties of Czernik 41 and NGC 1342. The contours in the two-dimensional joint posterior distributions represent confidence levels of 68%, 90%, and 95%. In the one-dimensional posterior distributions, vertical lines indicate the median as well as the 16th and 84th percentile confidence intervals. The CMDs of the OCs are displayed on the right side of the corner plots. Black dots correspond to the most probable member stars. The red solid lines are the PARSEC isochrones derived from the median values of the posterior distributions, and green dashed lines indicate calculated age errors of the OCs.

we adopted the value estimated from the relation described in Equations 3 and 4 in this study. Determining cluster ages and reddened distance modulus emphasized main-sequence stars, turn-off points, and red giants with $P \geq 0.5$. This ensured precise age estimation while identifying the PARSEC isochrones that best represent the clusters, incorporating their metallicities and high-probability member stars. The shifts were applied in the $U - B$ and $B - V$ color indices using the color excess values $E(U - B)$ and $E(B - V)$, as well as in apparent magnitudes using the distance modulus equation $\mu_0 = V - M_V - A_V = 5 \times \log d - 5$ (where A_V is the extinction coefficient in V band and d is the distance to the Sun). The uncertainties in the cluster ages were determined by encompassing all high-probability member stars and defining lower and upper age bounds that align with the observed data. The analysis yielded reddened distance moduli for the Czernik 41 and NGC 1342 as $m_V - M_V = 16.594 \pm 0.128$ and $m_V - M_V = 9.880 \pm 0.136$ mag, respectively. These correspond to de-reddened distances of $d_{\text{iso}} = 2485 \pm 151$ pc for Czernik 41 and $d_{\text{iso}} = 645 \pm 42$ pc for NGC 1342. The uncertainties in the distance moduli and distances were calculated using the equations provided in Carraro et al. (2017). The results are presented in Table 8. The PARSEC isochrones, representing the best-fit parameters for reddened distance moduli and ages, along with the $V \times (U - B)$ and $V \times (B - V)$ CMDs of Czernik 41 and NGC 1342, are presented in Figure 13.

5. KINEMATIC AND ORBITAL ANALYSIS

Radial velocity (V_R) measurements are essential parameters for the kinematic and orbital dynamics analysis of OCs. In this study, the mean radial velocities of Czernik 41 and NGC 1342 were determined using V_R data from the *Gaia* DR3 catalog. Stars within the clusters' limiting radii ($r_{\text{lim}} \leq 11'$) and with membership probabilities $P \geq 0.5$ were selected for the analysis. The *Gaia* DR3 catalog contained V_R measurements for seven stars in Czernik 41 and 43 stars in NGC 1342. Weighted mean values were calculated to derive the clusters' $\langle V_R \rangle$, using equations provided by Soubiran et al. (2018). The $\langle V_R \rangle$ of Czernik 41 was determined as 2.41 ± 1.92 km s $^{-1}$, while for NGC 1342 it was calculated as -10.48 ± 0.20 km s $^{-1}$. The determination of the space velocity components and Galactic orbits of the clusters was performed using the *MWPotential2014* algorithm from the *galpy* library (Bovy 2015). For Czernik 41 and NGC 1342, the input parameters for calculating the space velocity components and Galactic orbit parameters included equatorial coordinates, radial velocities derived in this study, mean proper motion (PM) components, distances from

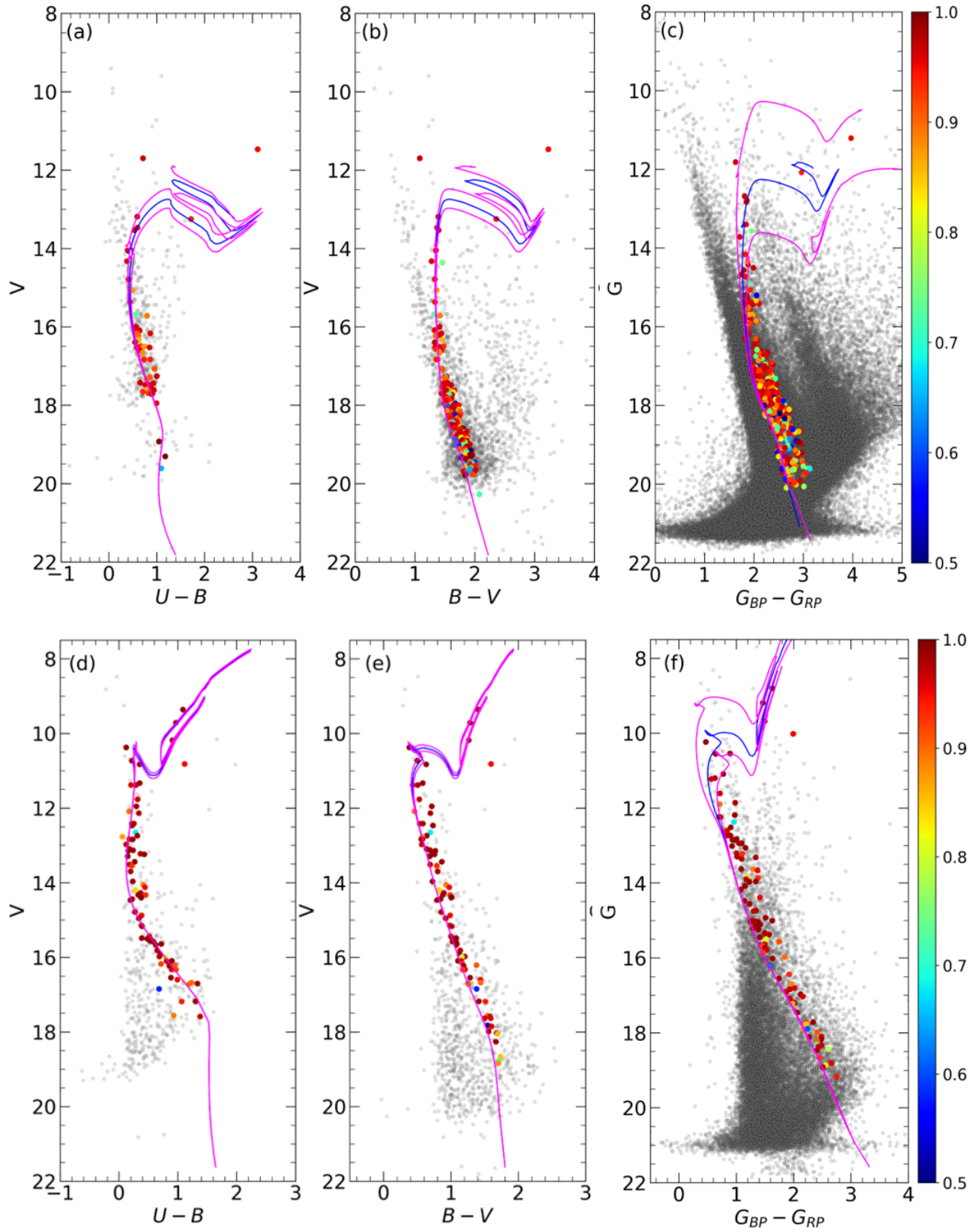


Figure 13. *UBV* and *Gaia* based CMDs for Czernik 41 (panels a, b, c) and NGC 1342 (panels d, e, f). The blue solid lines are the PARSEC isochrones that best fit the observed data, providing estimates for the clusters' distance moduli and ages. Purple solid lines represent the uncertainties in the age estimates. The color scales and symbol meanings are consistent with those described in Figure 4.

main-sequence fitting, and their associated uncertainties. In the calculations, the distance of the Sun from the Galactic center was assumed to be $R_{\text{gc}} = 8$ kpc, with a rotational velocity of $V_{\text{rot}} = 220$ km s $^{-1}$ (Bovy 2015; Bovy & Tremaine 2012), and a vertical distance from the Galactic plane of 27 ± 4 pc (Chen et al. 2000).

The orbital integrations of Czernik 41 and NGC 1342 were performed by tracing their current positions backwards in time for 2.5 Gyr with time steps of 1 Myr. From the analysis, key orbital parameters were determined, including the Galactocentric distance (R_{gc}), apogalactic (R_{a}) and perigalactic (R_{p}) distances from the Galactic center, orbital eccentricities (e), maximum vertical distances from the Galactic plane (z_{max}), space velocity components (U , V , W), and orbital periods (T_{p}).

The traceback early orbital radius (R_{teo}) method, recently introduced to the literature by Akbaba et al. (2024), has demonstrated that the birth regions of celestial objects within the Galaxy can be determined by tracing their past orbital paths under the assumption of a static Galactic potential. In contrast to the concept of the birth radius (R_{birth}), which aims to determine the formation sites of astronomical objects within the Galaxy based on Galactic chemical evolution models involving numerous assumptions (c.f., Minchev et al. 2018; Lu et al. 2024), the traceback early orbital radius (R_{teo}) provides information about the orbital position of an object's birth region by considering its present-day astrometric data and age. In this study, the calculation of R_{teo} was performed alongside other kinematic and dynamical parameters. The dynamical orbital parameters computed for the two clusters are listed in Table 8.

The space velocity components (U , V , W) for Czernik 41 were calculated as $(71.90 \pm 4.41, -35.73 \pm 2.36, -7.03 \pm 1.01)$ km s $^{-1}$. Similarly, for NGC 1342, the values were found to be $(8.24 \pm 0.19, -8.32 \pm 0.29, -0.44 \pm 0.24)$ km s $^{-1}$. The components of space velocity are influenced both by the stars' positions within the Milky Way and by inherent observational deviations from the Sun. To mitigate these biases, corrections for differential rotation and adjustments to the local standard of rest (LSR) were applied to each space velocity component. In particular, the differential rotation effects for the Czernik 41 and NGC 1342 were corrected using the relations presented in Mihalas & Binney (1981). This procedure yielded velocity corrections (dU , dV) as $(59.69, 2.80)$ km s $^{-1}$ for Czernik 41 and $(7.17, -1.35)$ km s $^{-1}$ for NGC 1342. Since the W space velocity component is unaffected by differential rotation no correction was necessary. For the LSR adjustment, the solar motion values from Coşkunoğlu et al. (2011), namely $(U, V, W)_{\odot} = (8.83 \pm 0.24, 14.19 \pm 0.34, 6.57 \pm 0.21)$ km s $^{-1}$ were applied

to adjust the space velocity components after differential velocity corrections were made. The total space velocities (S_{LSR}) of both OCs were obtained using the relation $S_{\text{LSR}} = \sqrt{U_{\text{LSR}}^2 + V_{\text{LSR}}^2 + W_{\text{LSR}}^2}$, with results presented in Table 8. The S_{LSR} values indicate that both clusters are associated with the young thin-disc stellar population (Leggett 1992).

The Galactic orbits of Czernik 41 and NGC 1342 are shown in Figure 14, concerning their vertical distance from the Galactic plane (Z) and the distance from the Galactic center (R_{gc}). Additionally, the evolution of the clusters' distance from the Galactic center over time ($R_{\text{gc}} \times t$) is presented (e.g. Taşdemir & Yontan 2023; Yontan & Canbay 2023c; Yücel et al. 2025). Panels a and c illustrate the motion of the clusters within the Galaxy as a function of their distance from the R_{gc} and the Z , respectively. Panels b and d depict the change in the clusters' distance from the Galactic center as a function of time (e.g. Yücel et al. 2024; Evcil et al. 2024; Elsanhoury et al. 2025). The current and early orbital positions of Czernik 41 and NGC 1342 are represented by yellow-filled circles and triangles, respectively, in Figure 14. The dashed pink and green lines, along with the corresponding triangles, illustrate the orbits and early orbital positions of the clusters, accounting for the upper and lower bounds of the input parameter errors. The upper panels of the figure demonstrate that Czernik 41 originated within the solar circle, following an orbit entirely traced within this region. In contrast, the lower panels of Figure 14 show that NGC 1342 formed outside the solar circle and subsequently entered it, also fully tracing this path. The uncertainties in the ages of the OCs further influence their early orbital positions. The age uncertainties were determined to be 10 Myr for Czernik 41 and 50 Myr for NGC 1342. Taking these age uncertainties into account, the variation in the R_{teo} positions for both clusters is represented by the shaded regions in the right panels of Figure 14. Dynamical orbital analysis reveal that, when considering age uncertainties, the early orbital positions of clusters could vary within the ranges approximately $6.45 \leq R_{\text{gc}} \leq 6.90$ for Czernik 41 and $8.60 \leq R_{\text{gc}} \leq 8.95$ for NGC 1342. Results support the inference of birth regions for both clusters.

The calculated Galactic orbit parameters of the two OCs were considered to determine their Galactic population types. The Galactic orbits of Czernik 41 and NGC 1342 exhibit eccentricities that do not exceed 0.08, with a maximum distances from the Galactic plane of $Z_{\text{max}} = 12 \pm 2$ pc and $Z_{\text{max}} = 192 \pm 8$ pc, respectively. These results also suggest that both OCs belong

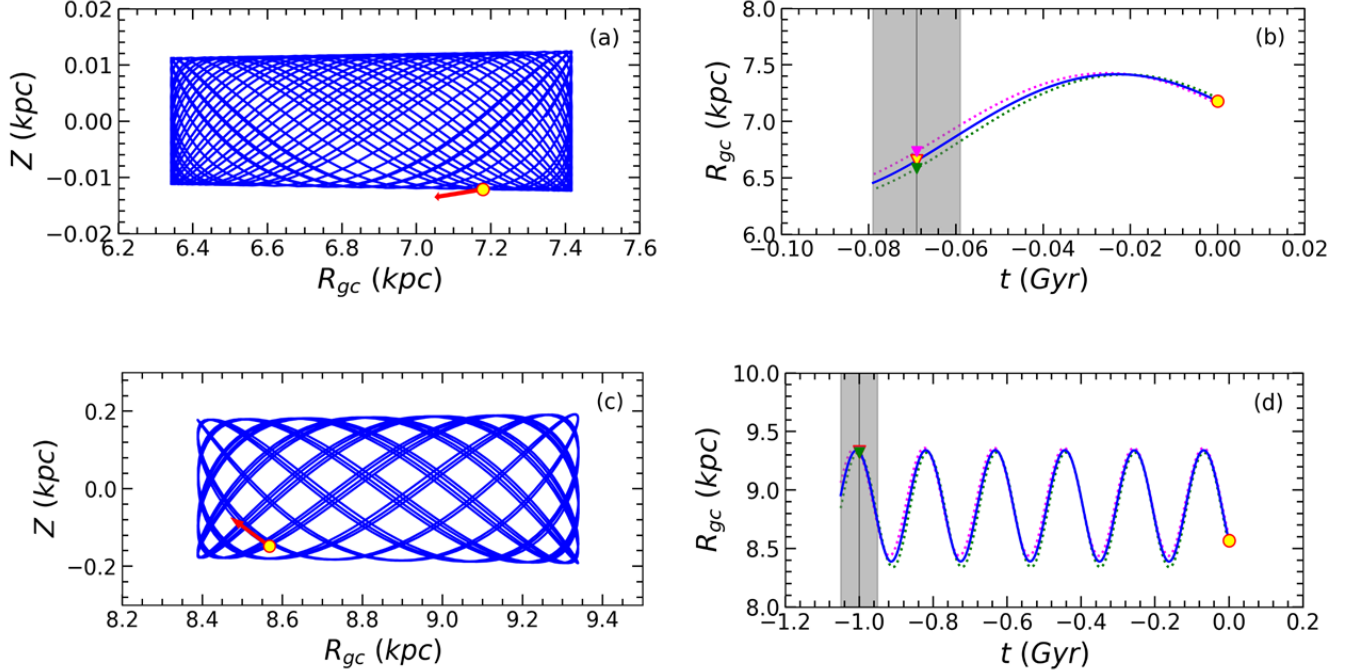


Figure 14. The distances of Czernik 41 (a, b) and NGC 1342 (c, d) from the Galactic center, along with their orbital trajectories perpendicular to the Galactic plane, are presented. The yellow-filled circles and triangles represent the current and early orbital positions of the clusters, respectively, while the red arrows indicate the direction of motion vectors of the OCs. The red-shaded regions in the right panels illustrate the uncertainty areas associated with the ages of the OCs. The vertical solid lines correspond to the ages of both OCs, marking their respective early orbital positions.

to the thin disk of the Galaxy (Plevne et al. 2015; Tunçel Güçtekin et al. 2019).

6. INVESTIGATING THE DYNAMICAL BEHAVIOR OF THE CLUSTERS

6.1. Luminosity and Mass Functions

In this study, the luminosity functions (LF) of both OCs were determined using main-sequence stars within the limiting radius defined for each cluster. The LFs of Czernik 41 and NGC 1342 were calculated using the cluster catalogs created in the *Gaia* system. To recap, the limiting radii of the OCs are $11'$, and the apparent magnitude range of the main-sequence stars with membership probabilities $P \geq 0.5$ within this region is $12 \leq G \text{ (mag)} \leq 20$ for Czernik 41 and $11 \leq G \text{ (mag)} \leq 19$ for NGC 1342. The absolute magnitudes M_G of these stars were calculated using the equation $M_G = G - 5 \times \log d + 1.8626 \times E(G_{BP} - G_{RP})$ (Cardelli et al. 1989; O'Donnell 1994), where d is the distance estimated above from the main-sequence fitting. As a result of these calculations, the M_G ranges for the stars in Czernik 41 and NGC 1342 were found to be $-1.5 < M_G \text{ (mag)} \leq 5.5$ and $1.4 < M_G \text{ (mag)} \leq 9.5$, respectively. The histograms of the LFs were then con-

structed by counting the number of stars corresponding to the unit M_G ranges (Figure 15). From Figure 15, it can be observed that in Czernik 41 (a) and NGC 1342 (b), the number of stars increases up to M_G of 3 and 6 mag, respectively, and then decreases after these magnitudes.

Additionally, the present-day mass functions (PDMFs) of both OCs were derived. The stellar masses were determined from the theoretical PARSEC models used in this study for the determination of the clusters' ages and distance moduli (Bressan et al. 2012). The data files from the PARSEC models include both the absolute magnitudes and mass values of the stars across various photometric systems. A polynomial function was applied to establish a relationship between the absolute magnitudes and stellar masses. These mass-luminosity relations were independently derived for each cluster and used to calculate the masses of the main-sequence stars identified in the LF analysis. The mass ranges for the main-sequence stars in Czernik 41 and NGC 1342 were determined to be $1.05 < M/M_\odot < 5.20$ and $0.40 < M/M_\odot < 1.85$, respectively. The G -band apparent magnitudes corresponding to these mass intervals span from 12 to 20 mag for Czernik 41, and

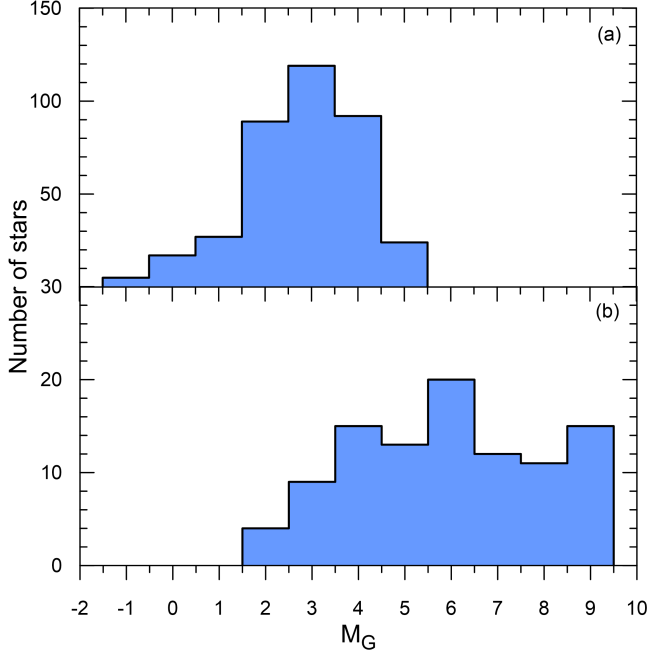


Figure 15. The histograms of LFs for Czernik 41 (a) and NGC 1342 (b).

from 11 to 19 mag for NGC 1342. It is worth noting that photometry is expected to be complete even for the fainter stars in these magnitude ranges, supporting the robustness of the PDMF analysis. For the calculation of the PDMFs, the stellar mass distributions were first generated. The stars were grouped into mass bins of $0.1M/M_\odot$ in both clusters. The logarithmic values of the number of stars in each mass bin were then calculated. These mass distributions are shown in Figure 16. The errors in the stellar mass values were computed using Poisson statistics ($1/\sqrt{N}$). For the determination of the clusters' PDMFs, the linear relation of $\log(\frac{dN}{dM}) = -(1+\Gamma) \times \log M + \text{constant}$ from Salpeter (1955) was applied. dN represents the number of stars per unit mass dM , M is the central mass of the stars, and Γ denotes the slope of the PDMF. The relationship used for the mass values is represented by a blue solid line in Figure 16. The slopes of the PDMFs for Czernik 41 and NGC 1342 were determined to be $\Gamma = 1.67 \pm 0.23$ and $\Gamma = 1.56 \pm 0.41$, respectively. These values are in agreement with the Salpeter (1955) value of $\Gamma = 1.35$.

6.2. The Dynamical State of Mass Segregation

Mass segregation, the process by which more massive stars tend to concentrate towards the center of a star cluster over time, is a fundamental aspect of the dynamical evolution of stellar systems. This phenomenon is driven by gravitational interactions among the stars within the cluster, and it is closely tied to relaxation pro-

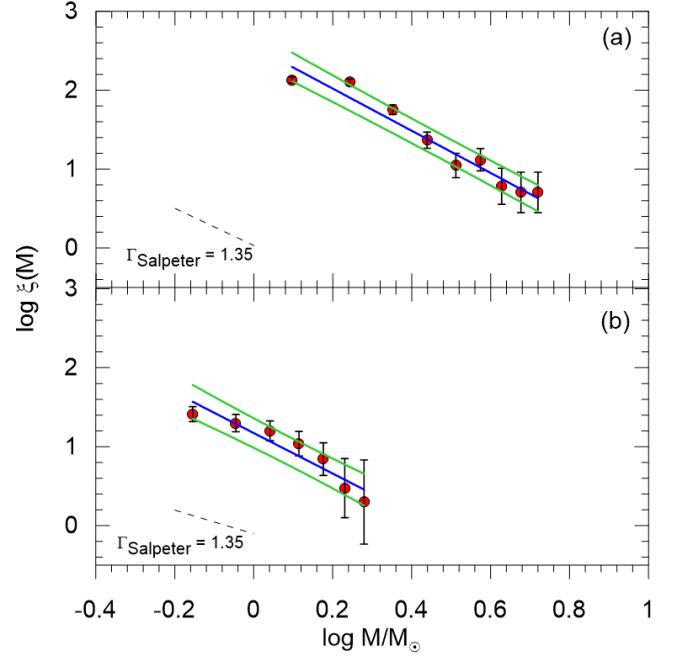


Figure 16. For Czernik 41 (a) and NGC 1342 (b), the mass distributions (red points) are shown along with the blue linear line applied to the distribution. The green lines indicate the prediction levels ($\pm 1\sigma$) of the linear fit.

cesses occurring over time (Sagar et al. 1988; Raboud & Mermilliod 1998; Fischer et al. 1998). The relaxation time, often referred to as the half-mass relaxation time (T_E), represents the characteristic time scale over which a cluster's stars undergo significant dynamical interactions. The interactions between cluster stars cause energy transfer from high-mass stars to low-mass stars, resulting in more massive stars gradually moving toward the cluster center while lower-mass stars move toward the cluster halo (see, e.g., Heggie 1979; Hillenbrand & Hartmann 1998; Baumgardt & Makino 2003; Dib & Henning 2019; Bisht et al. 2020; Pavlík & Vesperini 2022). This time is crucial in determining the extent of mass segregation in a cluster. This energy exchange process leads to kinetic energy equipartition, where the velocity distribution of stars conforms to a Maxwellian distribution. The T_E is crucial in determining the extent of mass segregation in a cluster, as it dictates how quickly the stars redistribute within the cluster. T_E depends on several factors, including the number of stars (N), the half-mass radius (in parsecs) of the cluster (R_h), and the mean mass of the stars ($\langle m \rangle$). It is given by Spitzer & Hart (1971) and typically expressed as:

$$T_E = \frac{8.9 \times 10^5 N^{1/2} R_h^{3/2}}{\langle m \rangle^{1/2} \log(0.4N)} \quad (14)$$

The connection between relaxation time and mass segregation is further complicated by the cluster’s age and the presence of external influences, such as tidal interactions or stellar feedback (Kruijssen et al. 2012). In younger clusters, primordial mass segregation may dominate, as the stars are still settling into their equilibrium distribution. As clusters age, the relaxation process becomes more significant, and the stars gradually redistribute in a way that leads to further mass segregation, particularly in denser regions. Studies of mass segregation in OCs indicate that the dynamical state of a cluster plays a pivotal role in determining its observed mass segregation (Allison et al. 2009; Haroon et al. 2025). For example, younger clusters, or those with short relaxation times, may exhibit strong central concentrations of massive stars, while older clusters with longer relaxation times may show a more uniform distribution due to the effects of dynamical relaxation. This suggests that the degree of mass segregation in a cluster is not only influenced by its initial conditions but also by its evolutionary state.

In our analysis of both OCs examined in this study, we determined their relaxation times and compared them with the observed degree of mass segregation. Our sample selection included stars with membership probabilities of $P \geq 0.5$ and those located within the limiting radius of each cluster. Based on these criteria, we identified 382 stars in Czernik 41 and 111 stars in NGC 1342, with mass ranges of $1.05 < M/M_\odot \leq 9.90$ for Czernik 41 and $0.40 < M/M_\odot \leq 2.25$ for NGC 1342. The total mass of Czernik 41 was estimated as $M = 771 M_\odot$, while for NGC 1342, it was found to be $M = 112 M_\odot$. This corresponds to a mean stellar mass of $\langle m \rangle = 2.02 M/M_\odot$ for Czernik 41 and $\langle m \rangle = 1.01 M/M_\odot$ for NGC 1342. The half-mass radii were determined as $R_h = 3.54$ pc for Czernik 41 and $R_h = 0.85$ pc for NGC 1342. The estimated dynamical relaxation times are $T_E = 37.31$ Myr for Czernik 41 and $T_E = 4.44$ Myr for NGC 1342. Since the relaxation times are significantly shorter than the present-day ages of both OCs, as derived in this study (see Table 8), we conclude that both OCs have reached a state of dynamical relaxation. However, the relaxation time values presented in this study should be considered as lower limits. They are based solely on stars detected within the photometric completeness range. The presence of unresolved low-mass stars and binary systems may increase the total mass and number of stars, thereby extending the estimated relaxation time. Therefore, for Czernik 41, it is possible that the relaxation time could be longer than the cluster age, implying that the cluster may not yet be fully relaxed dynamically.

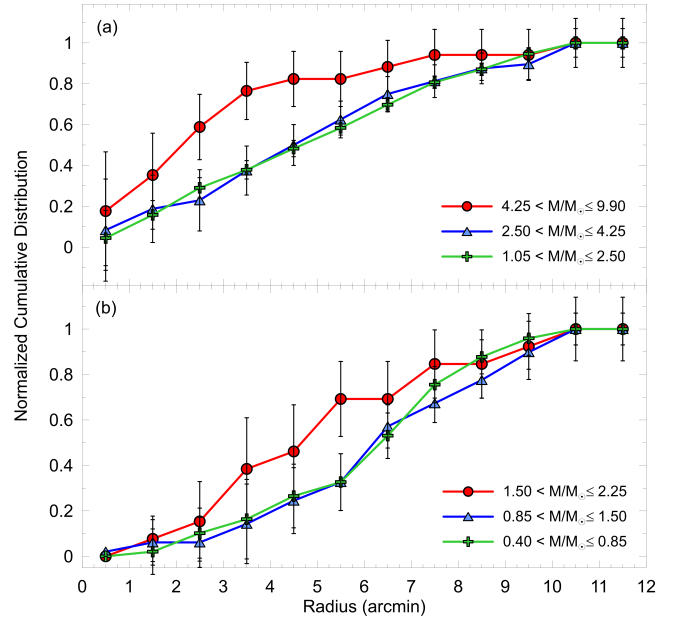


Figure 17. The cumulative radial distribution of stars across various mass ranges for Czernik 41 (a) and NGC 1342 (b).

To understand the impact of the mass segregation effect in both OCs, we divided the masses of selected stars into three intervals containing almost an equal number of stars. The mass intervals are $1.10 < M/M_\odot \leq 2.50$ (low-mass), $2.50 < M/M_\odot \leq 4.25$ (intermediate-mass), and $4.25 < M/M_\odot \leq 9.90$ (high-mass) for Czernik 41 and $1.50 < M/M_\odot \leq 2.25$, $0.85 < M/M_\odot \leq 1.50$, and $0.40 < M/M_\odot \leq 0.85$ for NGC 1342. The normalized cumulative radial distributions of cluster membership stars in these different mass intervals are shown in Figure 17. As shown in this figure, high-mass stars are concentrated in a region near the center of the OCs, whereas intermediate- and low-mass stars exhibit a similar distribution beyond the central region in both OCs.

To quantify this segregation, we applied the two-sided Kolmogorov–Smirnov (K–S) test to compare the radial distributions of high-mass stars with those of the other mass groups. The resulting confidence levels of 95% for Czernik 41 and 92% for NGC 1342 indicate that the null hypothesis (stating that the compared populations are drawn from the same parent distribution) can be rejected at these significance levels. These results provide statistical evidence that in these clusters the high-mass stars are distributed differently from the lower-mass stars, consistent with the presence of mass segregation in both OCs.

7. SUMMARY AND CONCLUSION

This study presents a comprehensive analysis of the photometric, astrometric, and spectroscopic data of the

Table 8. Fundamental parameters of Czernik 41 and NGC 1342.

Parameter	Czernik 41	NGC 1342
$(\alpha, \delta)_{J2000}$ (Sexagesimal)	19:51:01.0, +25:17:24	03:31:34.6, +37:22:48
$(l, b)_{J2000}$ (Decimal)	062.0238, -00.6899	154.9402, -15.3463
f_0 (stars arcmin ⁻²)	7.622 ± 0.750	1.733 ± 0.240
f_{bg} (stars arcmin ⁻²)	4.481 ± 0.171	1.766 ± 0.090
r_c (arcmin)	1.728 ± 0.266	2.155 ± 0.568
r_{lim} (arcmin)	11	11
r (pc)	7.95	2.06
C	0.804 ± 0.062	0.708 ± 0.102
Cluster members ($P \geq 0.5$)	382	111
$\mu_\alpha \cos \delta$ (mas yr ⁻¹)	-2.963 ± 0.068	0.419 ± 0.041
μ_δ (mas yr ⁻¹)	-6.163 ± 0.101	-1.662 ± 0.031
ϖ (mas)	0.381 ± 0.048	1.523 ± 0.051
d_ϖ (pc)	2625 ± 331	657 ± 22
$E(B - V)$ (mag)	1.500 ± 0.035	0.270 ± 0.043
$E(U - B)$ (mag)	1.080 ± 0.025	0.194 ± 0.031
A_V (mag)	4.650 ± 0.109	0.837 ± 0.133
$E(G_{BP} - G_{RP})$ (mag)	1.986 ± 0.295	0.290 ± 0.118
A_G (mag)	3.700 ± 0.550	0.540 ± 0.220
[Fe/H] (dex)	0.07 ± 0.09	-0.14 ± 0.07
Z	0.0176 ± 0.0038	0.0112 ± 0.0018
$m_V - M_V$ (mag)	16.594 ± 0.128	9.880 ± 0.136
d_{iso} (pc)	2485 ± 151	645 ± 42
Age (Myr)	69 ± 10	1000 ± 50
$(X, Y, Z)_\odot$ (pc)	(1166, 2194, -30)	(-563, 264, -171)
R_{gc} (pc)	7178 ± 27	8568 ± 37
PDMF slope	1.67 ± 0.23	1.56 ± 0.41
V_R (km s ⁻¹)	2.41 ± 1.92	-10.48 ± 0.20
U_{LSR} (km s ⁻¹)	20.71 ± 4.42	9.57 ± 0.31
V_{LSR} (km s ⁻¹)	-25.15 ± 2.38	6.41 ± 0.45
W_{LSR} (km s ⁻¹)	-0.54 ± 1.03	6.05 ± 0.32
S_{LSR} (km s ⁻¹)	32.58 ± 5.12	13.01 ± 0.63
R_a (pc)	7417 ± 6	9341 ± 19
R_p (pc)	6341 ± 34	8390 ± 50
Z_{max} (pc)	12 ± 2	192 ± 8
e	0.078 ± 0.002	0.054 ± 0.002
P_{orb} (Myr)	190 ± 1	250 ± 1
R_{teo} (kpc)	6.65 ± 0.07	9.32 ± 0.01

Czernik 41 and NGC 1342 OCs using CCD *UBV* observations and the *Gaia* DR3 catalog (Gaia Collaboration et al. 2023). Astrophysical, kinematical, and dynamical Galactic orbital parameters were derived exclusively from stars with a membership probability of $P \geq 0.5$. A key objective of this study is to investigate parameter degeneracy by applying both classical and MCMC methods to photometric and astrometric data. The consistency between the results obtained with both classical and MCMC methods demonstrated the reliability of

the derived astrophysical parameters. The results of the study are summarized as follows:

1) The RDPs were fitted with King (1962) models to derive structural parameters. The limiting radius for each cluster was visually set at $11'$, beyond which field stars dominate. Low central concentration, as indicated by the concentration parameters $C = 0.804 \pm 0.062$ for Czernik 41 and $C = 0.708 \pm 0.102$ for NGC 1342, may be characteristic of either dynamically young clusters that have not yet undergone significant mass segregation, or

dynamically evolved clusters that have experienced mass loss and core expansion

2) Membership selection was refined using both astrometric (UPMASK) and photometric criteria. For Czernik 41 and NGC 1342, 382, and 111 probable members ($P \geq 0.5$) were identified from *Gaia* DR3, while *UBV* photometry identified 172 and 89 members, respectively. The consistency between both selected criteria, with stars aligning along ZAMS-constrained regions, ensures a reliable basis for astrophysical parameter determination.

3) Proper motion distributions and vectorial motions revealed a denser stellar population in Czernik 41 compared to NGC 1342. The mean proper motion components ($\langle \mu_\alpha \cos \delta, \mu_\delta \rangle$) were $(-2.963 \pm 0.068, -6.163 \pm 0.101)$ mas yr $^{-1}$ for Czernik 41 and $(0.419 \pm 0.041, -1.662 \pm 0.031)$ mas yr $^{-1}$ for NGC 1342, consistent with the VPD of membership-selected stars. Mean trigonometric parallaxes ($\langle \varpi \rangle$) were 0.381 ± 0.048 and 1.523 ± 0.051 mas for Czernik 41 and NGC 1342, corresponding to distances (d_ϖ) to be 2625 ± 331 and 657 ± 22 pc, respectively.

4) Reddening and metallicity of both OCs were estimated using different methods. For Czernik 41, reddening was derived from the TCD as $E(B - V) = 1.500 \pm 0.035$ mag. Due to the absence of suitable F-G main-sequence stars, metallicity was determined via an MCMC-based technique, yielding $[\text{Fe}/\text{H}] = 0.07 \pm 0.09$ dex. The color excess and metallicity were obtained from TCDs, with $E(B - V) = 0.270 \pm 0.043$ mag and $[\text{Fe}/\text{H}] = -0.14 \pm 0.07$ dex for NGC 1342. These results show the methodological differences, particularly the use of MCMC for Czernik 41 due to the lack of metallicity-sensitive stars in *UBV* data.

5) Distances and ages of both OCs were determined using *UBV*-based PARSEC isochrones and MCMC analysis with *Gaia* DR3. $V \times (U - B)$ and $V \times (B - V)$ CMDs were constructed for stars with $P \geq 0.5$, yielding distance moduli (μ_V) of 16.594 ± 0.128 mag for Czernik 41 and 9.880 ± 0.136 mag for NGC 1342, corresponding to distances (d_{iso}) of 2485 ± 151 pc and 645 ± 42 pc. The ages (t) were determined as 69 ± 10 Myr for Czernik 41 and 1000 ± 50 Myr for NGC 1342. MCMC provided an independent estimate of these parameters, accounting for parameter degeneracies (see Table 8). The posterior distributions of A_G , d , Z , and $\log t$ were consistent with the *UBV*-based results, confirming the reliability of both methods.

6) The radial velocity measurements of OC member stars from the *Gaia* DR3 catalog were used to determine the mean radial velocities of the OCs. The mean radial velocities of Czernik 41 and NGC 1342 were calculated

to be 2.41 ± 1.92 (from 7 stars) and -10.48 ± 0.20 km s $^{-1}$ (from 43 stars), respectively.

7) The Galactic orbital analysis of both OCs revealed distinct orbital paths. Czernik 41, originating within the solar circle, remains within this region, while NGC 1342, formed outside the solar circle, has since entered it. Also, the estimated Z_{max} of Czernik 41 and NGC 1342 are smaller than 200 pc, indicating that both OCs are members of the thin disk.

8) The PDMF slopes were $\Gamma = 1.67 \pm 0.23$ for Czernik 41 and $\Gamma = 1.56 \pm 0.41$ for NGC 1342, falling within 1.4σ of the Salpeter (1955) value, indicating a typical stellar mass distribution for both OCs.

9) The relaxation times for Czernik 41 and NGC 1342 were calculated as 37.31 Myr and 4.44 Myr, respectively, suggesting that both clusters have likely reached dynamical relaxation. However, for Czernik 41, this value should be considered a lower limit due to incompleteness in low-mass and binary star detections. Thus, its actual relaxation time may exceed its age, implying that it might not yet be fully dynamically relaxed. Mass segregation analysis showed high-mass stars concentrated at the center, while lower-mass stars were more evenly distributed.

Software: Astrometry.net (Lang et al. 2010), Galpy (Bovy 2015), IRAF (Tody 1986, 1993), PyRAF (Science Software Branch at STScI 2012), SExtractor (Bertin & Arnouts 1996), UPMASK (Krone-Martins & Moitinho 2014).

ACKNOWLEDGMENTS

We would like to express our sincere gratitude to the anonymous referee for his/her valuable comments and suggestions, which were helpful in improving the quality of the manuscript. This study has been supported in part by the Scientific and Technological Research Council (TÜBİTAK) 122F109. Funding was provided by the Scientific Research Projects Coordination Unit of Istanbul University as project numbers FYL-2022-39160 and 40044. We thank TÜBİTAK for partial support towards using the T100 telescope via project 18CT100-1396. We also thank the on-duty observers and members of the technical staff at the TÜBİTAK National Observatory for their support before and during the observations. This study is a part of the MSc thesis of Burçin Tanık Öztürk. We also made use of Vizier and Simbad databases at CDS, Strasbourg, France. We made use of data from the European Space Agency (ESA) mission *Gaia*⁸, processed by the *Gaia* Data Processing and Analysis Consortium (DPAC)⁹. Funding for DPAC has been provided by national institutions, in particular the institutions participating in the *Gaia* Multilateral Agreement. We are grateful for the analysis system IRAF, which was distributed by the National Optical Astronomy Observatory (NOAO). NOAO was operated by the Association of Universities for Research in Astronomy (AURA) under a cooperative agreement with the National Science Foundation. PyRAF is a product of the Space Telescope Science Institute, which is operated by AURA for NASA. We thank the University of Queensland for the collaboration software.

REFERENCES

- Ak, T., Bostancı, Z. F., Yontan, T., et al. 2016, *Ap&SS*, 361, 126, doi: [10.1007/s10509-016-2707-2](https://doi.org/10.1007/s10509-016-2707-2)
- Ak, T., Canbay, R., & Yontan, T. 2024, *Physics and Astronomy Reports*, 2, 58, doi: [10.26650/PAR.2024.00006](https://doi.org/10.26650/PAR.2024.00006)
- Akbaba, F., Ak, T., Bilir, S., et al. 2024, *Astronomische Nachrichten*, 345, e20240052, doi: [10.1002/asna.20240052](https://doi.org/10.1002/asna.20240052)
- Akbulut, B., Ak, S., Yontan, T., et al. 2021, *Astrophysics and Space Science*, 366, 68, doi: [10.1007/s10509-021-03975-x](https://doi.org/10.1007/s10509-021-03975-x)
- Allison, R. J., Goodwin, S. P., Parker, R. J., et al. 2009, *ApJL*, 700, L99, doi: [10.1088/0004-637X/700/2/L99](https://doi.org/10.1088/0004-637X/700/2/L99)
- Bahcall, J. N., & Soneira, R. M. 1980, *ApJS*, 44, 73, doi: [10.1086/190685](https://doi.org/10.1086/190685)
- Bailer-Jones, C. A. L., Rybizki, J., Fouesneau, M., Demleitner, M., & Andrae, R. 2021, *AJ*, 161, 147, doi: [10.3847/1538-3881/abd806](https://doi.org/10.3847/1538-3881/abd806)
- Banks, T., Yontan, T., Bilir, S., & Canbay, R. 2020, *Journal of Astrophysics and Astronomy*, 41, 6, doi: [10.1007/s12036-020-9621-2](https://doi.org/10.1007/s12036-020-9621-2)
- Bastian, N., & Lardo, C. 2018, *ARA&A*, 56, 83, doi: [10.1146/annurev-astro-081817-051839](https://doi.org/10.1146/annurev-astro-081817-051839)
- Baumgardt, H., & Makino, J. 2003, *MNRAS*, 340, 227, doi: [10.1046/j.1365-8711.2003.06286.x](https://doi.org/10.1046/j.1365-8711.2003.06286.x)
- Bertin, E., & Arnouts, S. 1996, *A&AS*, 117, 393, doi: [10.1051/aas:1996164](https://doi.org/10.1051/aas:1996164)
- Bilir, S., Güver, T., Khamitov, I., et al. 2010, *Ap&SS*, 326, 139, doi: [10.1007/s10509-009-0233-1](https://doi.org/10.1007/s10509-009-0233-1)
- Bilir, S., Bostancı, Z. F., Yontan, T., et al. 2016, *Advances in Space Research*, 58, 1900, doi: [10.1016/j.asr.2016.06.039](https://doi.org/10.1016/j.asr.2016.06.039)

- Bisht, D., Zhu, Q., Yadav, R. K. S., Durgapal, A., & Rangwal, G. 2020, *MNRAS*, 494, 607, doi: [10.1093/mnras/staa656](https://doi.org/10.1093/mnras/staa656)
- Bostancı, Z. F., Ak, T., Yontan, T., et al. 2015, *MNRAS*, 453, 1095, doi: [10.1093/mnras/stv1665](https://doi.org/10.1093/mnras/stv1665)
- Bostancı, Z. F., Yontan, T., Bilir, S., et al. 2018, *Ap&SS*, 363, 143, doi: [10.1007/s10509-018-3364-4](https://doi.org/10.1007/s10509-018-3364-4)
- Bovy, J. 2015, *The Astrophysical Journal Supplement Series*, 216, 29, doi: [10.1088/0067-0049/216/2/29](https://doi.org/10.1088/0067-0049/216/2/29)
- Bovy, J., & Tremaine, S. 2012, *The Astrophysical Journal*, 756, 89, doi: [10.1088/0004-637X/756/1/89](https://doi.org/10.1088/0004-637X/756/1/89)
- Bressan, A., Marigo, P., Girardi, L., et al. 2012, *Monthly Notices of the Royal Astronomical Society*, 427, 127, doi: [10.1111/j.1365-2966.2012.21948.x](https://doi.org/10.1111/j.1365-2966.2012.21948.x)
- Cameron, L. M. 1985, *A&A*, 147, 39
- Cantat-Gaudin, T., & Anders, F. 2020, *A&A*, 633, A99, doi: [10.1051/0004-6361/201936691](https://doi.org/10.1051/0004-6361/201936691)
- Cantat-Gaudin, T., Jordi, C., Vallenari, A., et al. 2018, *Astronomy and Astrophysics*, 618, A93, doi: [10.1051/0004-6361/201833476](https://doi.org/10.1051/0004-6361/201833476)
- Cantat-Gaudin, T., Anders, F., Castro-Ginard, A., et al. 2020, *Astronomy and Astrophysics*, 640, A1, doi: [10.1051/0004-6361/202038192](https://doi.org/10.1051/0004-6361/202038192)
- Cardelli, J. A., Clayton, G. C., & Mathis, J. S. 1989, *ApJ*, 345, 245, doi: [10.1086/167900](https://doi.org/10.1086/167900)
- Carraro, G., Sales Silva, J. V., Moni Bidin, C., & Vazquez, R. A. 2017, *The Astronomical Journal*, 153, 99, doi: [10.3847/1538-3881/153/3/99](https://doi.org/10.3847/1538-3881/153/3/99)
- Castro-Ginard, A., McMillan, P. J., Luri, X., et al. 2021, *A&A*, 652, A162, doi: [10.1051/0004-6361/202039751](https://doi.org/10.1051/0004-6361/202039751)
- Çakmak, H., Yontan, T., Bilir, S., et al. 2024, *Astronomische Nachrichten*, 345, e20240054, doi: [10.1002/asna.20240054](https://doi.org/10.1002/asna.20240054)
- Çınar, D. C., Tasdemir, S., Koc, S., & Iyer, S. 2024, *Physics and Astronomy Reports*, 2, 1, doi: [10.26650/PAR.2024.00002](https://doi.org/10.26650/PAR.2024.00002)
- Chen, Y. Q., Nissen, P. E., Zhao, G., Zhang, H. W., & Benoni, T. 2000, *A&AS*, 141, 491, doi: [10.1051/aas:2000124](https://doi.org/10.1051/aas:2000124)
- Conrad, C., Scholz, R. D., Kharchenko, N. V., et al. 2017, *A&A*, 600, A106, doi: [10.1051/0004-6361/201630012](https://doi.org/10.1051/0004-6361/201630012)
- Coşkunoglu, B., Ak, S., Bilir, S., et al. 2011, *Monthly Notices of the Royal Astronomical Society*, 412, 1237, doi: [10.1111/j.1365-2966.2010.17983.x](https://doi.org/10.1111/j.1365-2966.2010.17983.x)
- Cui, X.-Q., Zhao, Y.-H., Chu, Y.-Q., et al. 2012, *Research in Astronomy and Astrophysics*, 12, 1197, doi: [10.1088/1674-4527/12/9/003](https://doi.org/10.1088/1674-4527/12/9/003)
- Czernik, M. 1966, *AcA*, 16, 93
- Deng, L.-C., Newberg, H. J., Liu, C., et al. 2012, *Research in Astronomy and Astrophysics*, 12, 735, doi: [10.1088/1674-4527/12/7/003](https://doi.org/10.1088/1674-4527/12/7/003)
- Dias, W. S., Monteiro, H., Moitinho, A., et al. 2021, *Monthly Notices of the Royal Astronomical Society*, 504, 356, doi: [10.1093/mnras/stab770](https://doi.org/10.1093/mnras/stab770)
- Dias, W. S., Monteiro, H., Caetano, T. C., et al. 2014, *Astronomy and Astrophysics*, 564, A79, doi: [10.1051/0004-6361/201323226](https://doi.org/10.1051/0004-6361/201323226)
- Dib, S., & Henning, T. 2019, *A&A*, 629, A135, doi: [10.1051/0004-6361/201834080](https://doi.org/10.1051/0004-6361/201834080)
- Eker, Z., & Bakış, V. 2025, *Physics and Astronomy Reports*, 3, 43, doi: [10.26650/PAR.2025.00005](https://doi.org/10.26650/PAR.2025.00005)
- Eker, Z., Soyduğan, F., & Bilir, S. 2024, *Physics and Astronomy Reports*, 2, 41, doi: [10.26650/PAR.2024.00001](https://doi.org/10.26650/PAR.2024.00001)
- Eker, Z., Soyduğan, F., Bilir, S., et al. 2020, *Monthly Notices of the Royal Astronomical Society*, 496, 3887, doi: [10.1093/mnras/staa1659](https://doi.org/10.1093/mnras/staa1659)
- Eker, Z., Bakış, V., Bilir, S., et al. 2018, *Monthly Notices of the Royal Astronomical Society*, 479, 5491, doi: [10.1093/mnras/sty1834](https://doi.org/10.1093/mnras/sty1834)
- Elsanhoury, W. H., Haroon, A. A., Elkholy, E. A., & Çınar, D. C. 2025, *Journal of Astrophysics and Astronomy*, 46, 21, doi: [10.1007/s12036-025-10044-0](https://doi.org/10.1007/s12036-025-10044-0)
- Elson, R., Hut, P., & Inagaki, S. 1987, *ARA&A*, 25, 565, doi: [10.1146/annurev.aa.25.090187.003025](https://doi.org/10.1146/annurev.aa.25.090187.003025)
- Evcil, S., Adalalı, S., Alan, N., Canbay, R., & Bilir, S. 2024, *Astronomische Nachrichten*, 345, e20240038, doi: [10.1002/asna.20240038](https://doi.org/10.1002/asna.20240038)
- Fischer, P., Pryor, C., Murray, S., Mateo, M., & Richtler, T. 1998, *AJ*, 115, 592, doi: [10.1086/300212](https://doi.org/10.1086/300212)
- Foreman-Mackey, D., Hogg, D. W., Lang, D., & Goodman, J. 2013, *PASP*, 125, 306, doi: [10.1086/670067](https://doi.org/10.1086/670067)
- Frinchaboy, P. M., Thompson, B., Jackson, K. M., et al. 2013, *ApJL*, 777, L1, doi: [10.1088/2041-8205/777/1/L1](https://doi.org/10.1088/2041-8205/777/1/L1)
- Fu, X., Bragaglia, A., Liu, C., et al. 2022, *A&A*, 668, A4, doi: [10.1051/0004-6361/202243590](https://doi.org/10.1051/0004-6361/202243590)
- Gaia Collaboration, Prusti, T., de Bruijne, J. H. J., et al. 2016, *A&A*, 595, A1, doi: [10.1051/0004-6361/201629272](https://doi.org/10.1051/0004-6361/201629272)
- Gaia Collaboration, Brown, A. G. A., Vallenari, A., et al. 2018, *Astronomy and Astrophysics*, 616, A1, doi: [10.1051/0004-6361/201833051](https://doi.org/10.1051/0004-6361/201833051)
- Gaia Collaboration, Vallenari, A., Brown, A. G. A., et al. 2023, *A&A*, 674, A1, doi: [10.1051/0004-6361/202243940](https://doi.org/10.1051/0004-6361/202243940)
- Garcia, B., Claria, J. J., & Levato, H. 1988, *Ap&SS*, 143, 317, doi: [10.1007/BF00637143](https://doi.org/10.1007/BF00637143)
- Gokmen, S., Eker, Z., Yontan, T., et al. 2023, *AJ*, 166, 263, doi: [10.3847/1538-3881/ad08b0](https://doi.org/10.3847/1538-3881/ad08b0)
- Hao, C. J., Xu, Y., Wu, Z. Y., et al. 2022, *A&A*, 668, A13, doi: [10.1051/0004-6361/202244570](https://doi.org/10.1051/0004-6361/202244570)

- Hao, C. J., Xu, Y., Hou, L. G., et al. 2021, *A&A*, 652, A102, doi: [10.1051/0004-6361/202140608](https://doi.org/10.1051/0004-6361/202140608)
- Haroon, A. A., Elsanhoury, W. H., Elkholy, E. A., Saad, A. S., & Çınar, D. C. 2025, *PhysS*, 100, 055006, doi: [10.1088/1402-4896/adb7f1](https://doi.org/10.1088/1402-4896/adb7f1)
- Heggie, D. C. 1979, *Monthly Notices of the Royal Astronomical Society*, 188, 525, doi: [10.1093/mnras/188.3.525](https://doi.org/10.1093/mnras/188.3.525)
- Herschel, W. 1802, *Phil. Trans. R. Soc.*, 92, 477, doi: <https://doi.org/10.1098/rstl.1802.0021>
- Hidayat, W., Arifyanto, M. I., Aprilia, & Hakim, M. I. 2019, in *Journal of Physics Conference Series*, Vol. 1231, *Journal of Physics Conference Series (IOP)*, 012032, doi: [10.1088/1742-6596/1231/1/012032](https://doi.org/10.1088/1742-6596/1231/1/012032)
- Hill, A., & Zaritsky, D. 2006, *AJ*, 131, 414, doi: [10.1086/498647](https://doi.org/10.1086/498647)
- Hillenbrand, L. A., & Hartmann, L. W. 1998, *ApJ*, 492, 540, doi: [10.1086/305076](https://doi.org/10.1086/305076)
- Hoag, A. A., Johnson, H. L., Iriarte, B., et al. 1961, *Publ. Us. Nav. Obs. XVII part VII*, 17, 347
- Janes, K., Barnes, S. A., Meibom, S., & Hoq, S. 2013, *AJ*, 145, 7, doi: [10.1088/0004-6256/145/1/7](https://doi.org/10.1088/0004-6256/145/1/7)
- Joshi, Y. C., Deepak, & Malhotra, S. 2024, *Frontiers in Astronomy and Space Sciences*, 11, 1348321, doi: [10.3389/fspas.2024.1348321](https://doi.org/10.3389/fspas.2024.1348321)
- Karaali, S., Ak, S. G., Bilir, S., Karataş, Y., & Gilmore, G. 2003a, *Monthly Notices of the Royal Astronomical Society*, 343, 1013, doi: [10.1046/j.1365-8711.2003.06743.x](https://doi.org/10.1046/j.1365-8711.2003.06743.x)
- Karaali, S., Bilir, S., Ak, S., Yaz, E., & Coşkunoglu, B. 2011, *Publications of the Astronomical Society of Australia*, 28, 95, doi: [10.1071/AS10026](https://doi.org/10.1071/AS10026)
- Karaali, S., Bilir, S., Karataş, Y., & Ak, S. G. 2003b, *Publications of the Astronomical Society of Australia*, 20, 165, doi: [10.1071/AS02028](https://doi.org/10.1071/AS02028)
- Kharchenko, N. V., Piskunov, A. E., Röser, S., Schilbach, E., & Scholz, R. D. 2005, *Astronomy and Astrophysics*, 438, 1163, doi: [10.1051/0004-6361:20042523](https://doi.org/10.1051/0004-6361:20042523)
- Kharchenko, N. V., Piskunov, A. E., Schilbach, E., Röser, S., & Scholz, R. D. 2012, *A&A*, 543, A156, doi: [10.1051/0004-6361/201118708](https://doi.org/10.1051/0004-6361/201118708)
- Kharchenko, N. V., Piskunov, A. E., Schilbach, E., Röser, S., & Scholz, R. D. 2013, *Astronomy and Astrophysics*, 558, A53, doi: [10.1051/0004-6361/201322302](https://doi.org/10.1051/0004-6361/201322302)
- King, I. 1962, *Astronomical Journal*, 67, 471, doi: [10.1086/108756](https://doi.org/10.1086/108756)
- Koç, S., Yontan, T., Bilir, S., et al. 2022, *The Astronomical Journal*, 163, 191, doi: [10.3847/1538-3881/ac58a0](https://doi.org/10.3847/1538-3881/ac58a0)
- Krone-Martins, A., & Moitinho, A. 2014, *Astronomy and Astrophysics*, 561, A57, doi: [10.1051/0004-6361/201321143](https://doi.org/10.1051/0004-6361/201321143)
- Kruijssen, J. M. D., Maschberger, T., Moeckel, N., et al. 2012, *MNRAS*, 419, 841, doi: [10.1111/j.1365-2966.2011.19748.x](https://doi.org/10.1111/j.1365-2966.2011.19748.x)
- Lada, C. J., & Lada, E. A. 2003, *ARA&A*, 41, 57, doi: [10.1146/annurev.astro.41.011802.094844](https://doi.org/10.1146/annurev.astro.41.011802.094844)
- Landolt, A. U. 2009, *The Astronomical Journal*, 137, 4186, doi: [10.1088/0004-6256/137/5/4186](https://doi.org/10.1088/0004-6256/137/5/4186)
- Lang, D., Hogg, D. W., Mierle, K., Blanton, M., & Roweis, S. 2010, *AJ*, 139, 1782, doi: [10.1088/0004-6256/139/5/1782](https://doi.org/10.1088/0004-6256/139/5/1782)
- Leggett, S. K. 1992, *Astrophysical Journal Supplement*, 82, 351, doi: [10.1086/191720](https://doi.org/10.1086/191720)
- Liu, L., & Pang, X. 2019, *The Astrophysical Journal Supplement Series*, 245, 32, doi: [10.3847/1538-4365/ab530a](https://doi.org/10.3847/1538-4365/ab530a)
- Loktin, A. V., & Beshenov, G. V. 2003, *Astronomy Reports*, 47, 6, doi: [10.1134/1.1538491](https://doi.org/10.1134/1.1538491)
- Loktin, A. V., & Popova, M. E. 2017, *Astrophysical Bulletin*, 72, 257, doi: [10.1134/S1990341317030154](https://doi.org/10.1134/S1990341317030154)
- Lu, Y. L., Minchev, I., Buck, T., et al. 2024, *MNRAS*, 535, 392, doi: [10.1093/mnras/stae2364](https://doi.org/10.1093/mnras/stae2364)
- Maciejewski, G., & Niedzielski, A. 2007, *A&A*, 467, 1065, doi: [10.1051/0004-6361:20066588](https://doi.org/10.1051/0004-6361:20066588)
- Marshall, D. J., Robin, A. C., Reylé, C., Schultheis, M., & Picaud, S. 2006, *A&A*, 453, 635, doi: [10.1051/0004-6361:20053842](https://doi.org/10.1051/0004-6361:20053842)
- Maurya, J., & Joshi, Y. C. 2020, *MNRAS*, 494, 4713, doi: [10.1093/mnras/staa893](https://doi.org/10.1093/mnras/staa893)
- McKee, C. F., & Ostriker, E. C. 2007, *ARA&A*, 45, 565, doi: [10.1146/annurev.astro.45.051806.110602](https://doi.org/10.1146/annurev.astro.45.051806.110602)
- Medina, G. E., Lemasle, B., & Grebel, E. K. 2021, *MNRAS*, 505, 1342, doi: [10.1093/mnras/stab1267](https://doi.org/10.1093/mnras/stab1267)
- Mermilliod, J. C., Mayor, M., & Udry, S. 2008, *A&A*, 485, 303, doi: [10.1051/0004-6361:200809664](https://doi.org/10.1051/0004-6361:200809664)
- Mihalas, D., & Binney, J. 1981, *Galactic astronomy. Structure and kinematics (W.H. Freeman & Co.)*
- Minchev, I., Anders, F., Recio-Blanco, A., et al. 2018, *MNRAS*, 481, 1645, doi: [10.1093/mnras/sty2033](https://doi.org/10.1093/mnras/sty2033)
- Miocchi, P., Lanzoni, B., Ferraro, F. R., et al. 2013, *ApJ*, 774, 151, doi: [10.1088/0004-637X/774/2/151](https://doi.org/10.1088/0004-637X/774/2/151)
- Muñoz, R. R., Geha, M., & Willman, B. 2010, *AJ*, 140, 138, doi: [10.1088/0004-6256/140/1/138](https://doi.org/10.1088/0004-6256/140/1/138)
- Netopil, M., Oralhan, İ. A., Çakmak, H., Michel, R., & Karataş, Y. 2022, *MNRAS*, 509, 421, doi: [10.1093/mnras/stab2961](https://doi.org/10.1093/mnras/stab2961)
- O'Donnell, J. E. 1994, *ApJ*, 422, 158, doi: [10.1086/173713](https://doi.org/10.1086/173713)
- Pavlik, V., & Vesperini, E. 2022, *MNRAS*, 515, 1830, doi: [10.1093/mnras/stac1776](https://doi.org/10.1093/mnras/stac1776)
- Peña, J. H., Peniche, R., Bravo, H., & Yam, O. 1994, *RMxAA*, 28, 7

- Piskunov, A. E., Kharchenko, N. V., Röser, S., Schilbach, E., & Scholz, R. D. 2006, *A&A*, 445, 545, doi: [10.1051/0004-6361:20053764](https://doi.org/10.1051/0004-6361:20053764)
- Plevne, O., Ak, T., Karaali, S., et al. 2015, *PASA*, 32, e043, doi: [10.1017/pasa.2015.44](https://doi.org/10.1017/pasa.2015.44)
- Portegies Zwart, S. F., McMillan, S. L. W., & Gieles, M. 2010, *ARA&A*, 48, 431, doi: [10.1146/annurev-astro-081309-130834](https://doi.org/10.1146/annurev-astro-081309-130834)
- Raboud, D., & Mermilliod, J. C. 1998, *A&A*, 333, 897, doi: [10.48550/arXiv.astro-ph/9802284](https://doi.org/10.48550/arXiv.astro-ph/9802284)
- Rangwal, G., Arya, A., Subramaniam, A., Singh, K. P., & Liu, X. 2024, arXiv e-prints, arXiv:2410.15305, doi: [10.48550/arXiv.2410.15305](https://doi.org/10.48550/arXiv.2410.15305)
- Reddy, A. B. S., Giridhar, S., & Lambert, D. L. 2015, *MNRAS*, 450, 4301, doi: [10.1093/mnras/stv908](https://doi.org/10.1093/mnras/stv908)
- . 2020, *Journal of Astrophysics and Astronomy*, 41, 38, doi: [10.1007/s12036-020-09658-3](https://doi.org/10.1007/s12036-020-09658-3)
- Robin, A. C., Reylé, C., Derrière, S., & Picaud, S. 2003, *A&A*, 409, 523, doi: [10.1051/0004-6361:20031117](https://doi.org/10.1051/0004-6361:20031117)
- Robin, A. C., Luri, X., Reylé, C., et al. 2012, *A&A*, 543, A100, doi: [10.1051/0004-6361/201118646](https://doi.org/10.1051/0004-6361/201118646)
- Roeser, S., Demleitner, M., & Schilbach, E. 2010, *AJ*, 139, 2440, doi: [10.1088/0004-6256/139/6/2440](https://doi.org/10.1088/0004-6256/139/6/2440)
- Ruprecht, J. 1966, *Bulletin of the Astronomical Institutes of Czechoslovakia*, 17, 33
- Sagar, R., Miakutin, V. I., Piskunov, A. E., & Dluhnevskaja, O. B. 1988, *MNRAS*, 234, 831, doi: [10.1093/mnras/234.4.831](https://doi.org/10.1093/mnras/234.4.831)
- Salpeter, E. E. 1955, *ApJ*, 121, 161, doi: [10.1086/145971](https://doi.org/10.1086/145971)
- Sarajedini, A., Milone, A. A. E., & Lowe, C. R. 1995, in *American Astronomical Society Meeting Abstracts*, Vol. 186, American Astronomical Society Meeting Abstracts #186, 49.03
- Schlafly, E. F., & Finkbeiner, D. P. 2011, *ApJ*, 737, 103, doi: [10.1088/0004-637X/737/2/103](https://doi.org/10.1088/0004-637X/737/2/103)
- Science Software Branch at STScI. 2012, PyRAF: Python alternative for IRAF, *Astrophysics Source Code Library*, record ascl:1207.011
- Sestito, P., Bragaglia, A., Randich, S., et al. 2008, *A&A*, 488, 943, doi: [10.1051/0004-6361:200809650](https://doi.org/10.1051/0004-6361:200809650)
- Skrutskie, M. F., Cutri, R. M., Stiening, R., et al. 2006, *AJ*, 131, 1163, doi: [10.1086/498708](https://doi.org/10.1086/498708)
- Soubiran, C., Cantat-Gaudin, T., Romero-Gómez, M., et al. 2018, *Astronomy and Astrophysics*, 619, A155, doi: [10.1051/0004-6361/201834020](https://doi.org/10.1051/0004-6361/201834020)
- Spina, L., Magrini, L., & Cunha, K. 2022, *Universe*, 8, 87, doi: [10.3390/universe8020087](https://doi.org/10.3390/universe8020087)
- Spitzer, L. 1987, *Dynamical evolution of globular clusters*
- Spitzer, Jr., L., & Hart, M. H. 1971, *ApJ*, 164, 399, doi: [10.1086/150855](https://doi.org/10.1086/150855)
- Strobel, A. 1991a, *Astronomische Nachrichten*, 312, 177, doi: [10.1002/asna.2113120306](https://doi.org/10.1002/asna.2113120306)
- . 1991b, *A&A*, 247, 35
- Sung, H., Lim, B., Bessell, M. S., et al. 2013, *Journal of Korean Astronomical Society*, 46, 103, doi: [10.5303/JKAS.2013.46.3.103](https://doi.org/10.5303/JKAS.2013.46.3.103)
- Taşdemir, S., Çınar, D. C., Canbay, R., et al. 2025, *Physics and Astronomy Reports*, 3, 1, doi: [10.26650/PAR.2025.00003](https://doi.org/10.26650/PAR.2025.00003)
- Taşdemir, S., & Yontan, T. 2023, *Physics and Astronomy Reports*, 1, 1, doi: [10.26650/PAR.2023.00001](https://doi.org/10.26650/PAR.2023.00001)
- Tarricq, Y., C., S., Casamiquela, L., et al. 2021, *Astronomy and Astrophysics*, 647, A19, doi: [10.1051/0004-6361/202039388](https://doi.org/10.1051/0004-6361/202039388)
- Tody, D. 1986, in *Society of Photo-Optical Instrumentation Engineers (SPIE) Conference Series*, Vol. 627, *Instrumentation in astronomy VI*, ed. D. L. Crawford, 733, doi: [10.1117/12.968154](https://doi.org/10.1117/12.968154)
- Tody, D. 1993, in *Astronomical Society of the Pacific Conference Series*, Vol. 52, *Astronomical Data Analysis Software and Systems II*, ed. R. J. Hanisch, R. J. V. Brissenden, & J. Barnes, 173
- Tunçel Güçtekin, S., Bilir, S., Karaali, S., Plevne, O., & Ak, S. 2019, *Advances in Space Research*, 63, 1360, doi: [10.1016/j.asr.2018.10.041](https://doi.org/10.1016/j.asr.2018.10.041)
- Vázquez, R. A., Moitinho, A., Carraro, G., & Dias, W. S. 2010, *A&A*, 511, A38, doi: [10.1051/0004-6361/200811583](https://doi.org/10.1051/0004-6361/200811583)
- Virtanen, P., Gommers, R., Oliphant, T. E., et al. 2020, *Nature Methods*, 17, 261, doi: [10.1038/s41592-019-0686-2](https://doi.org/10.1038/s41592-019-0686-2)
- Yontan, T. 2023a, *AJ*, 165, 79, doi: [10.3847/1538-3881/aca6f0](https://doi.org/10.3847/1538-3881/aca6f0)
- Yontan, T., Bilir, S., Çakmak, H., et al. 2023b, *Advances in Space Research*, 72, 1454, doi: [10.1016/j.asr.2023.04.015](https://doi.org/10.1016/j.asr.2023.04.015)
- Yontan, T., & Canbay, R. 2023c, *Physics and Astronomy Reports*, 1, 65, doi: [10.26650/PAR.2023.00008](https://doi.org/10.26650/PAR.2023.00008)
- Yontan, T., Bilir, S., Bostancı, Z. F., et al. 2015, *Ap&SS*, 355, 267, doi: [10.1007/s10509-014-2175-5](https://doi.org/10.1007/s10509-014-2175-5)
- . 2019, *Ap&SS*, 364, 152, doi: [10.1007/s10509-019-3640-y](https://doi.org/10.1007/s10509-019-3640-y)
- Yontan, T., Bilir, S., Ak, T., et al. 2021, *Astronomische Nachrichten*, 342, 538, doi: [10.1002/asna.202113837](https://doi.org/10.1002/asna.202113837)
- Yontan, T., Çakmak, T., Bilir, S., et al. 2022, *RMxAA*, 58, 333, doi: [10.22201/ia.01851101p.2022.58.02.14](https://doi.org/10.22201/ia.01851101p.2022.58.02.14)
- Yücel, G., Bakış, V., Canbay, R., et al. 2025, *AJ*, 169, 71, doi: [10.3847/1538-3881/ad9d46](https://doi.org/10.3847/1538-3881/ad9d46)
- Yücel, G., Canbay, R., & Bakış, V. 2024, *Physics and Astronomy Reports*, 2, 18, doi: [10.26650/PAR.2024.00003](https://doi.org/10.26650/PAR.2024.00003)
- Zacharias, N., Urban, S. E., Zacharias, M. I., et al. 2004, *AJ*, 127, 3043, doi: [10.1086/386353](https://doi.org/10.1086/386353)

Zhao, G., Zhao, Y.-H., Chu, Y.-Q., Jing, Y.-P., & Deng,
L.-C. 2012, *Research in Astronomy and Astrophysics*, 12,
723, doi: [10.1088/1674-4527/12/7/002](https://doi.org/10.1088/1674-4527/12/7/002)

Zhong, J., Chen, L., Wu, D., et al. 2020, *A&A*, 640, A127,
doi: [10.1051/0004-6361/201937131](https://doi.org/10.1051/0004-6361/201937131)
Zhou, X., & Chen, X. 2021, *MNRAS*, 504, 4768,
doi: [10.1093/mnr/stab1209](https://doi.org/10.1093/mnr/stab1209)